ChemPhotoChem

Review
doi.org/10.1002/cptc.202400024

Chemistry Europe
European Chemical Societies Publishing

www.chemphotochem.org

Internal Electric Fields and Structural Instabilities in Insulating Transition Metal Compounds: Influence on Optical Properties

I. Sánchez-Movellán,*[a] P. García-Fernández,[a] J. M. García-Lastra,[b] J. A. Aramburu,[a] and M. Moreno[a]

This work reviews new ideas developed in the last two decades which play a key role for understanding the optical properties of insulating materials containing transition metal (TM) cations. Initially, this review deals with compounds involving d^4 and d^9 ions where the local structure of the involved MX_6 complexes (M=d^n cation, X=ligand) is never cubic but distorted, a fact widely ascribed to the Jahn-Teller (JT) effect. Nevertheless, that assumption is often wrong as the JT coupling requires an orbitally degenerate ground state in the initial geometry a condition not fulfilled even if the lattice is tetragonal. For this reason, the equilibrium geometry of d^4 and d^9 complexes in low symmetry lattices, is influenced by two factors: (i) The effects, usually ignored, of the internal electric field, $\mathbf{E}_R$, due to the rest of lattice ions on the active electrons localized in the MX_6 unit. (ii) The existence of structural instabilities driven by vibronic interactions that lead to negative force constants. As first examples of these ideas, we show that the equilibrium structure, electronic ground state of $KZnF_3:Cu^{2+}$, $K_2ZnF_4:Cu^{2+}$ and K_2CuF_4 obey to different causes and only in $KZnF_3:Cu^{2+}$ the JT effect takes place. These ideas also explain the local structure and optical properties of CuF_2, CrF_2 or $KAlCuF_6$ compounds where the JT effect is symmetry forbidden and those of layered copper chloroperovskites where the orthorhombic instability explains the red shift of one *d–d* transition under pressure. In a second step, this review explores stable systems involving d^3, d^5 or d^9 cations, where the internal electric field, $\mathbf{E}_R$, is responsible for some puzzling phenomena. This is the case of ruby and emerald that surprisingly exhibit a different color despite the Cr^{3+}-O^{2-} distance is the same. A similar situation holds when comparing the normal ($KMgF_3$) and the inverted ($LiBaF_3$) perovskites doped with Mn^{2+} having the same Mn^{2+}-F distance but clearly different optical spectra. The role of $\mathbf{E}_R$ is particularly remarkable looking for the origin of the color in the historical Egyptian Blue pigment based on $CaCuSi_4O_{10}$.

1. Introduction

Insulating transition metal (TM) compounds are widely investigated due to the rich physical and chemical properties that appear following the open shell structure of the TM cation. For this reason, these compounds usually exhibit optical response in the V-UV domain and magnetic ordering below a given temperature. Research in this field is gaining increasing importance because of a detailed knowledge of the bulk and surface electronic structure is essential for understanding and optimizing the mechanisms relevant to the growing number of technological applications of these materials, which are used in lasers,[1–3] devices with colossal magnetoresistance,[4] solar cells[5] or systems displaying high piezochromism.[6,7]

In these materials active electrons are essentially *confined* in the MX_N complex formed by the transition metal cation, M, and the N nearest anions X.[8] Accordingly, it is widely assumed that many properties of TM compounds can be explained to a good extent just considering the *isolated* MX_N complex thus ignoring the rest of lattice ions.[9–11]

In the realm of TM compounds those involving d^9 cations play a singular role. Indeed, considering only the sixfold coordinated MX_6 complexes (M=Cu^{2+}, Ag^{2+}) present in such compounds they are always distorted from cubic symmetry.[10] The same situation happens for d^4 cations in high spin configuration and also for d^7 cations in low spin configuration. The existence of that distortion is usually ascribed to the Jahn-Teller (JT) effect.[12] However, that assumption is often hard to be accepted due to the restrictive conditions behind a JT effect.[8,13,14] Indeed, when we consider the complex actually embedded in the crystal lattice, it requires an orbitally degenerate electronic ground state in the initial high symmetry geometry (here denoted as *parent phase*). However, this rule is broken when the lattice geometry is tetragonal, orthorhombic, monoclinic or triclinic.

The present work is a review dealing with new ideas developed in the last two decades that improve our understanding of optical properties due to insulating compounds

[a] *I. Sánchez-Movellán, P. García-Fernández, J. A. Aramburu, M. Moreno*
Departamento de Ciencias de la Tierra y Física de la Materia Condensada
Universidad de Cantabria
Avenida de los Castros s/n, 39005 Santander, Spain
E-mail: sanchezi@unican.es

[b] *J. M. García-Lastra*
Department of Energy Conversion, Storage
Technical University of Denmark
Anker Engelunds Vej. Building 301, 2800 Kgs. Lyngby, Denmark

containing transition metal cations. Two main factors behind the equilibrium geometry and the associated optical excitations are: (i) The internal electric field, $\mathbf{E}_R$, due to the rest of lattice ions upon the active electrons localized in the MX_N unit[15,16] an important factor usually ignored within the ligand field theory (LFT) essentially focused on the isolated complex.[9–11] (ii) The existence of structural instabilities driven by a force constant that becomes negative,[17] a mechanism which is enhanced in pure compounds where nearest complexes share a common ligand.[18]

A first part of the present analysis is addressed to pure and doped fluorides containing d^9 cations. In this domain, we firstly explore three systems, Cu^{2+}-doped $KZnF_3$[19,20] and K_2ZnF_4[21,22] and pure K_2CuF_4[23,24] which are similar in composition but exhibit different optical properties as a result of a distinct equilibrium geometry and electronic ground state.[25] The present ideas also shed light on the local structure and optical properties of other compounds like CuF_2,[26–31] CrF_2[32–34] or $KAlCuF_6$[35–39] as well as of layered copper chloroperovskites[40–42] where often the longest Cu–Cl bond becomes extremely soft as a result of the orthorhombic instability.[43] This key fact gives rise to a surprising red shift of some *d*–*d* and charge transfer transitions under pressure.[6,7,41,43]

The second part of this work is devoted to compounds involving d^3, d^5 or d^9 cations without structural instabilities where the internal electric field, $\mathbf{E}_R$, is responsible for some puzzling phenomena. This is the case of ruby and emerald gemstones where the Cr^{3+}–O^{2-} distance is the same although such materials surprisingly exhibit a different color.[44–50] Along this line we also deal with two Mn^{2+}-doped crystals, a normal cubic perovskite $KMgF_3$[51,52] and the inverted perovskite $LiBaF_3$[53,54] which exhibit a clearly different crystal field spectrum despite the Mn^{2+}–F^- distances are identical[55] within 0.5 %.

Finally, we discuss the origin of the color in the historical Egyptian Blue pigment based on the $CaCuSi_4O_{10}$ compound.[56,57] In this material, Cu^{2+} cations do not display a sixfold but a fourfold coordination giving rise to stable square-planar CuO_4^{6-} complexes with a hole in the $b_{1g}(x^2\text{-}y^2)$ level. As a salient feature, it is shown that the existence of a very anisotropic internal field $\mathbf{E}_R$ produces a huge red shift of around 1 eV on the highest *d*–*d* transition, $a_{1g}(3z^2\text{-}r^2) \rightarrow b_{1g}(x^2\text{-}y^2)$, which is thus behind the blue color of the historical pigment.[58]

This review work is organized as follows. For the sake of clarity, section 2 offers a theoretical background mainly focused on the JT effect, the microscopic origin of structural instabilities and the relevance of the internal electric field, $\mathbf{E}_R$. Section 3 is devoted to the equilibrium geometry and optical properties of systems involving d^9 or d^4 cations while section 4 deals with stable insulating materials where the effects of the internal electric field play a key role.

Inés Sánchez-Movellán is a Ph.D. student at the University of Cantabria. She received her B. S. degree in Physics in 2019 and completed her M. S. studies in Theoretical Chemistry and Computational Modelling in 2021. Her research is focused on structural instabilities related to electron-nuclei interactions in insulating materials containing transition metal ions. She is also involved in the study of electronic, optical and magnetic properties of this kind of compounds.

Pablo Garcia-Fernandez received his B. S. degree and PhD from Universidad de Cantabria, Spain. He carried out a postdoctoral stay at the University of Texas at Austin (USA) with Profs. J. E. Boggs and I. B. Bersuker and later became a Ramón y Cajal fellow at Universidad de Cantabria. He is currently an associate professor at this institution. His main research involves the development of second-principles methods and the study of vibronic phenomena in solids, including their relationship with optical and magnetic properties.

Juan Maria García-Lastra received his B.S. degree and Ph.D. from the University of Cantabria, Spain. He completed his first postdoctoral fellowship at the University of the Basque Country (UPV/EHU) with Prof. Ángel Rubio through a Juan de la Cierva Fellowship. This was followed by a second postdoctoral fellowship at the Technical University of Denmark (DTU) with Prof. Kristian Thygesen through an Ørsted Fellowship. Subsequently, he was awarded a Ramón y Cajal Fellowship at UPV/EHU for a short period before returning to DTU. At DTU, he is now a professor and heads the Atomic Scale Modelling Materials Section at the Department of Energy. His primary research focuses on the theoretical study of materials for energy applications, such as photovoltaic materials and batteries, using ab initio methodologies.

José Antonio Aramburu obtained in 1985 his phD with Oustanding Prize from the University of Cantabria (UC) and continued his academic journey in the group of Prof. Miguel Moreno, focusing in the theoretical and computational study of the correlation of structural, optical and magnetic properties of solids containing transition metal cations. He got an associated professor in the Condensed Matter Physics Department of UC in 1989 and Full Professor in 2003. He is expert in qualitative and quantitative interpretation of experimental data of molecules and solids from rigorous ab initio theory and density functional theory calculations.

2. Theoretical Background

2.1. Electronic Density and the Jahn-Teller Effect

In pure and doped insulating compounds electrons are essentially localized.[8] For this reason, a good starting point for understanding the properties of $KNiF_3$ or K_2NaAlF_6:Cr^{3+} systems is simply to consider the NiF_6^{4-} or CrF_6^{3-} units, where active electrons are localized, at the right equilibrium distance.[8,9,11] This idea is correct provided the ground state of the complex is placed well below the bottom of the conduction band and the energy of first excitations (up to 6 eV) smaller than the band gap, E_g, of the crystal.[8] The last condition is specially fulfilled for fluorides involving E_g values higher than 10 eV.[59,60] In the singular system KCl:Ag^0 the situation is somewhat different as the 5s electron of silver is stabilized just below the bottom of the conduction band of KCl but only thanks to a huge outwards relaxation of ligands (~20%).[61,8]

In the cubic host lattice K_2NaAlF_6, Cr^{3+} impurities replace Al^{3+} cations[62,63] and the ground state of the octahedral CrF_6^{3-} complex, $^4A_2$, involves three unpaired electrons in the t_{2g} orbitals (Figure 1, left), thus the corresponding wavefunction, Ψ_0, can shortly be written as the Slater determinant, described in the abbreviated form following Ref. [11].

$$\Psi_0(M_S = 3/2) = |xy \uparrow xz \uparrow yz \uparrow| \quad (1)$$

Here *xy* actually means an antibonding molecular orbital of the CrF_6^{3-} complex transforming like xy under the O_h symmetry group. Accordingly, the electronic density in the ground state of CrF_6^{3-} can shortly be written as

$$\rho = \rho_{CS} + [(xy)^2 + (xz)^2 + (xz)^2] \quad (2)$$

where ρ_{CS} denotes the density from fully occupied orbitals (closed shells) of the CrF_6^{3-} complex which keeps cubic symmetry. As the electronic density coming from the three unpaired electrons is also a cubic invariant, in the $Al^{3+} \rightarrow Cr^{3+}$ substitution the six ligands move in the *same* way. Accordingly, the octahedral symmetry of the reference geometry is preserved although the metal-ligand distance can change following the different ionic radii of Al^{3+}, Cr^{3+}.

A different situation holds, however, when considering a Rh^{2+} impurity ($4d^7$ configuration) entering the cubic NaCl replacing Na^+, involving a *remote* defect that compensates for the excess of local positive charge.[64,65] In this case, the electronic ground state corresponds to the low spin ($S=^1/_2$) configuration $t_{2g}^6e_g^1$ (Figure 1, right) in perfect octahedral symmetry thus implying an orbitally degenerate ground state. Interestingly, if the unpaired electron is placed in the molecular orbital of the $RhCl_6^{4-}$ unit simply denoted as $3z^2$-r^2, the electronic density, ρ, is not compatible with cubic symmetry. Indeed, ρ can be written as[8,66]

$$\begin{aligned} \rho &= \rho_{CS} + \rho(3z^2\text{-}r^2) = \rho_{CS} + \rho_C + \rho_T \\ \rho_C &= (1/2)\ \{\rho(3z^2\text{-}r^2) + \rho(x^2\text{-}y^2)\} \sim 2(x^4 + y^4 + z^4) + \ldots \\ \rho_T &= (1/2)\ \{\rho(3z^2\text{-}r^2) - \rho(x^2\text{-}y^2)\} \sim 2z^4\text{-}\ (x^4 + y^4) + \ldots \end{aligned} \quad (3)$$

considering that $\rho(3z^2\text{-}r^2) \sim (3z^2\text{-}r^2)^2$ while[11] $\rho(x^2\text{-}y^2) \sim [\sqrt{3}\ (x^2\text{-}y^2)]^2$. In Eq. (3) ρ_{CS} describes the electronic density associated with t_{2g}^6 and other closed shells lying at lower energy.

Interestingly, ρ_{CS} and ρ_C exhibit cubic symmetry but ρ_T displays tetragonal symmetry giving rise to a *force* that moves outwards the two Cl^- ligands along the z-axis and inwards the four ligands in the XY plane (Figure 2a). Thus, the tetragonal density ρ_T generates the Q_ε distortion mode[13,14,67] (transforming like $3z^2$-r^2) described in terms of ionic displacements, u_i (i = 1, …, 6) as follows

$$Q_\theta = \frac{1}{\sqrt{12}}\{2(u_5 + u_6) - (u_1 + u_2 + u_3 + u_4)\} \quad (4)$$

When only this distortion mode is activated, this gives rise to an elongated tetragonal equilibrium geometry, with Z as main axis, described by $u_5 = u_6 = +2u$, $u_1 = u_2 = u_3 = u_4 = -u$ (Figure 2a). Obviously, an equivalent situation is reached placing the unpaired electron in the orbital $|3y^2\text{-}r^2\rangle = (-1/2)|3z^2\text{-}r^2\rangle - (\sqrt{3}/2)|x^2\text{-}y^2\rangle$ which would lead to a tetragonal distortion, with Y as main axis (Figure 2b), described by the mode $(-1/2)Q_\theta - (\sqrt{3}/2)Q_\varepsilon$ where Q_ε transforms like x^2-y^2 and is given by[13,14,67]

$$Q_\varepsilon = \frac{1}{2}\{u_1 - u_2 + u_3 - u_4\} \quad (5)$$

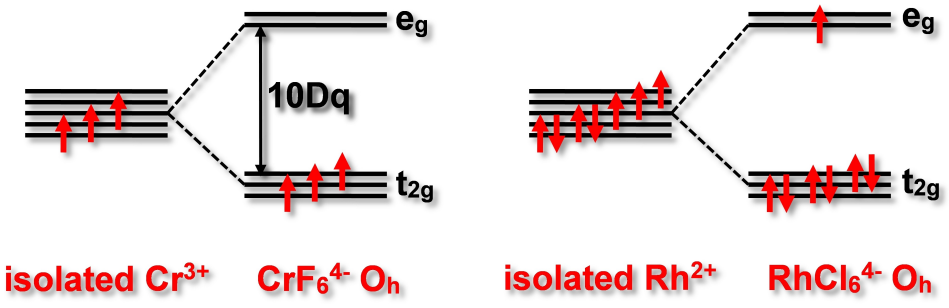

Figure 1. Left: splitting (called 10Dq) of 3d orbitals of a Cr^{3+} ion under the crystal field of a CrF_6^{3-} complex with octahedral symmetry. Right: splitting of the 4d orbitals of a Rh^{2+} ion under the crystal field of a $RhCl_6^{4-}$ complex with octahedral symmetry.

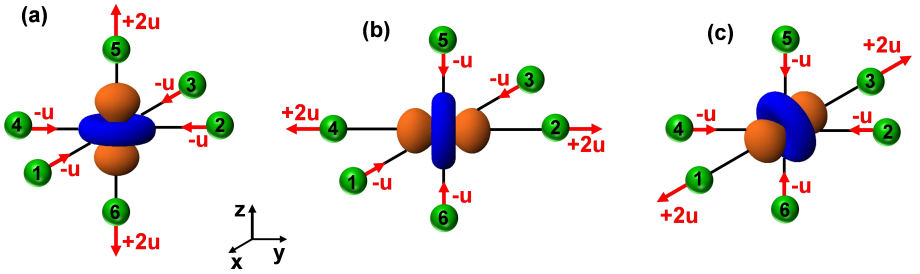

Figure 2. Tetragonal equilibrium geometry for an initially octahedral $RhCl_6^{4-}$ complex due to an unpaired electron in (a) $3z^2$-r^2, (b) $3y^2$-r^2 and (c) $3x^2$-r^2. The force on a ligand is parallel to the displacement (2u or –u). The Q_θ mode is described by red arrows in (a).

In the case of NaCl:Rh^{2+}, due to the initial cubic symmetry, another equivalent situation is found with the unpaired electron placed in the $3x^2$-r^2 orbital with X being then the main tetragonal axis (Figure 2c).

Although the three distortions with X, Y, Z as main axes are in principle equivalent such equivalence is however destroyed by the existence of random strains,[14] inevitably present in any real crystal,[13,68] making that at a given point of the lattice one of them is favored. This usual situation is termed static JT effect,[13,14] giving rise to three tetragonal centers, represented in Figure 2, that only differ in the nature of the main axis. The simultaneous existence of those three centers in NaCl:Rh^{2+} is well proved through Electron Paramagnetic Resonance (EPR) measurements.[64] Only in a few JT systems, like for MgO:Cu^{2+} [69,70] or MgO:Ag^{2+}[71] the existence of coherent tunnelling[13,72] among the three equivalent distortions (coherent dynamic JT effect) has been observed.

According to the initial degeneracy in NaCl:Rh^{2+} another possibility is to place the unpaired electron in the $|x^2\text{-}y^2\rangle$ molecular orbital of the $RhCl_6^{4-}$ unit, giving rise to a compressed tetragonal geometry at equilibrium. However, the anharmonicity, present in any molecular vibration, favors the elongated over the compressed conformation provided the complex is elastically decoupled from the rest of the lattice,[65,73,74] such as it happens for NaCl:Rh^{2+}. Among the cases involving a static JT effect and octahedral coordination in crystals, only in CaO:Ni^{+} the equilibrium geometry has been found to be purely compressed.[75,76] In this case the complex coming from the monovalent Ni^+ is, however, strongly coupled to the lattice made of *divalent* Ca^{2+} cations.

If we now consider a Cu^{2+} impurity in the cubic NaCl crystal the ground state of the $CuCl_6^{4-}$ unit in perfect O_h symmetry belongs to the $t_{2g}^6e_g^3$ configuration, thus involving a hole in the e_g level.[77] If, for instance, the hole is placed in the $|x^2\text{-}y^2\rangle$ orbital and we designate by $\rho_H(x^2\text{-}y^2)$ its associated density, then the electronic density of the electronic ground state, $\rho(t_{2g}^6e_g^3)$ verifies[66]

$$\rho(t_{2g}^6e_g^3) + \rho_H(x^2\text{-}y^2) = \rho_C \tag{6}$$

just underlining that $t_{2g}^6e_g^4$ is a closed shell. For this reason, the electronic density that generates the tetragonal distortion is $-\rho_H(x^2\text{-}y^2)$. Accordingly, a hole in the $|x^2\text{-}y^2\rangle$ orbital of the $CuCl_6^{4-}$ complex induces an elongated conformation whereas a compressed shape comes out when the hole is in $|3z^2\text{-}r^2\rangle$.

A precious information on the nature of the electronic ground state in static JT systems involving d^n ions (n = 9, 7, 4) is derived from the experimental g-tensor measured in EPR experiments provided covalency is low or moderate.[8,67] So, if $g_{||}-g_0 > g_\perp-g_0$ the unpaired electron lies in the $|x^2\text{–}y^2\rangle$ orbital while the opposite means that it is placed in $|3z^2\text{-}r^2\rangle$. As usual, $g_{||}$ is the gyromagnetic factor measured when the magnetic field, **H**, is parallel to the main axis of the tetragonal unit. The experimental values measured for NaCl:Rh^{2+} ($g_{|||}=2.019$, $g_\perp=2.451$)[64], NaCl:Cu^{2+} ($g_{|||}=2.373$, $g_\perp=2.070$)[77] prove that for both d^7, d^9 systems the equilibrium geometry corresponds to an elongated octahedron although the unpaired electron is located in a different orbital.

2.2. Linear Vibronic Coupling and the Jahn-Teller Effect

The previous ideas on the JT distortion as a result of the force acting on the ligands[66] are consistent with the usual description[14,67] through the coupling between nuclear vibrations and electrons (vibronic coupling). In this view, within the framework of perturbation theory, the total Hamiltonian, H, is divided into two contributions, one coming from the Hamiltonian, H_0, for frozen nuclei at the initial parent phase geometry and the other, H_{vib}, which introduces the linear vibronic coupling as a perturbation

$$H = H_0 + H_{vib} \approx H_0 + \Sigma_{\Gamma,j}\, V_{\Gamma,j}(\mathbf{r})\, Q_{\Gamma,j} \tag{7}$$

where summation runs on vibrational modes Γ with ionic displacements characterized by normal coordinates $Q_{\Gamma,j}$ where the index j accounts for the degeneracy of the Γ mode. $V_{\Gamma,j}(\mathbf{r})$, transforming like $Q_{\Gamma,j}$, is the vibronic coupling operator.[14]

In first-order perturbation, if the orbital wavefunction of the H_0 ground state belongs to the Γ_0 irrep it must be verified that $\Gamma_0\times\Gamma_0 \supset \Gamma$. For this reason, if the ground state is orbitally nondegenerate it can only be coupled with the symmetric mode that keeps the symmetry of the complex. By contrast, non-symmetric modes can be involved in first-order perturbation if the ground state is orbitally degenerate and this is just the essence of the JT effect.[8,13,14]

For the sake of clarity, we consider now a particular case of JT effect, namely $E_g \otimes e_g$, where the reference geometry configuration is octahedral and the electronic ground state E_g is orbitally two-fold degenerate. The effective vibronic Hamiltonian in this case can be written[14] in terms of the two degenerate nuclear motions (e_g symmetry) Q_θ, Q_ε (Eqs. (4), (5)),

$$H_{vib} = V_\theta(\mathbf{r})\ Q_\theta + V_\varepsilon(\mathbf{r})\ Q_\varepsilon \tag{8}$$

which describes the linear vibronic coupling, where $V_\theta \sim Q_\theta$, $V_\varepsilon \sim Q_\varepsilon$.

If we recall the case shown in the previous section, an impurity of Rh^{2+} in the pure NaCl lattice, it is an example of this $E_g \otimes e_g$ JT effect. If the unpaired e_g electron is placed in $3z^2$-r^2 orbital, one can calculate[78] the forces acting on ligands 1 and 5 when $Q_\theta = Q_\varepsilon = 0$. According to Eqs. (4), (8), considering that $\langle e_g(3z^2 - r^2)|V_\theta|e_g(3z^2 - r^2)\rangle = -V$, these forces are given by

$$F_Z(5) = -\partial E/\partial u_5 = -\langle e_g(3z^2 - r^2)|V_\theta|e_g(3z^2 - r^2)\rangle(\partial Q_\theta/\partial u_5) = \frac{2}{\sqrt{12}}\ V \tag{9}$$

$$F_X(1) = -\frac{1}{\sqrt{12}} V \tag{10}$$

showing that, for an impurity in a lattice site with octahedral symmetry in which an unpaired electron is localized in the $3z^2$-r^2 orbital, the forces over the ligands induce an elongated tetragonal distortion (Figure 2a), in full agreement with the results coming from the electronic density standpoint. As discussed in section 2.1, this tetragonal distortion is described by a Q_θ mode, which leads the system to an elongated tetragonal equilibrium geometry. The associated energy can be obtained, in a first step, by adding a harmonic elastic contribution[14] to the vibronic contribution coming from Eq. (8)

$$E = -V\ Q_\theta + \frac{1}{2}\ KQ_\theta^2 \tag{11}$$

where the force constant related to the elastic contribution is $K > 0$. It is important to note that we consider only the elastic, first-order vibronic terms, neglecting anharmonicity that is, however, inevitably present in any molecular vibration.[8,13,73] Under these conditions, the minimum energy configuration is found for $Q_\theta^0 = V/K$, which gives a stabilization energy E_{JT}

$$E_{JT} = -\frac{V^2}{2\ K} \tag{12}$$

According to Eq. (12), the stabilization energy is the same for both elongated and compressed geometries. However, the anharmonicity, which is present in any real crystal, plays a key role in favoring the stabilization of the elongated configuration over the compressed one, when the complex is elastically decoupled to a good extent from the rest of the lattice.[8,13,65,66] Interestingly, the energies of elongated and compressed conformations differ in a small quantity, known as the energy barrier B (Figure 3), that is usually in the range 0.01–0.1 eV.[8,13,79] The main factors governing the JT effect have recently been reviewed.[80,81]

The distortion throughout a tetragonal Q_θ mode gives rise to a lifting of E_g degeneracy characteristic of octahedral symmetry. Therefore, an energy gap appears between the two *d* levels $3z^2$-r^2, x^2-y^2. In particular, at the minimum Q_θ^0 (Figure 3) this energy gap between the ground and the first excited state has a value $\Delta E = 4|E_{JT}|$, which will give approximately the energy of the first *d*–*d* transition.[14,79] Considering that typical values of V and K are about 1 eV/Å, 5 eV/Å^2 respectively,[8,13] the JT stabilization energy, E_{JT}, will be around 0.1 eV, thus we will find the energy gap between $3z^2$-r^2, x^2-y^2 close to 0.4 eV. As it will be discussed in section 3.1, that figure is close to the estimated value for the transition $3z^2$-$r^2 \rightarrow x^2$-y^2 for Cu^{2+}-doped $KZnF_3$.

2.3. Vibronic Effects in an Orbitally Non-degenerate Ground State: Structural Instability

In the previous section we have seen that, in first-order perturbation, H_{vib} can couple a non-symmetric distortion mode to the ground state only if it is orbitally degenerate. However, if the ground state is an orbital singlet, new phenomena appear when considering the effects of H_{vib} (Eq. (8)) in second-order perturbations. In particular, this gives rise to a *negative contribution to the force constant* for the electronic ground state. If $\Psi_0(r)$ is the wavefunction of the ground state orbital singlet and Q_Γ is a non-symmetric, non-degenerate vibration mode, H_{vib} can couple $\Psi_0(r)$ with excited states, $\Psi_n(r)$, belonging to Γ_n. That admixture induces a change in the energy of the ground state given by[17,18]

$$\Delta E_0 = -Q^2 \sum_n \frac{\langle \Psi_0(r)|V_\Gamma(r)|\Psi_n(r)\rangle^2}{E_n - E_0} \tag{13}$$

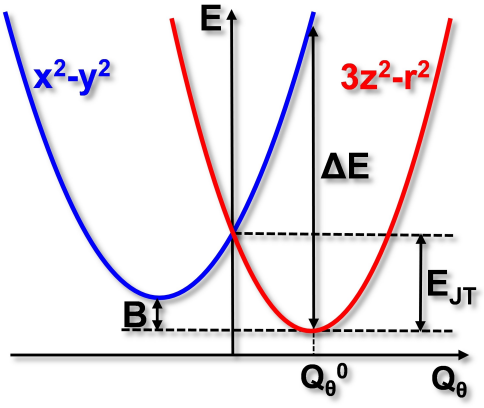

Figure 3. Electronic energies of elongated (red curve) and compressed (blue curve) conformations in the $E_g \otimes e_g$ JT effect for a d^9 octahedral complex depicted versus the tetragonal Q_θ deformation. Q_θ^0 is the equilibrium deformation, E_{JT} the JT stabilization energy in equilibrium, B the energy barrier between both conformations. The red curve shows the results for a ground state with an unpaired electron in the x^2-y^2 orbital while the blue curve corresponds to the unpaired electron in $3z^2$-r^2.

Thus, the excited states verifying $\Gamma_0 \times \Gamma_n \supset \Gamma$ can be coupled to the ground state modifying the electronic density and giving rise to a *negative* contribution to the force constant, $-K_v$, which can be written as

$$K = K_0 - K_v \tag{14}$$

Here K_0 stands for the positive contribution associate with the frozen electronic density of H_0 while K_v reflects the density changes due to H_{vib} and is given by[17]

$$K_V = 2\sum_n \frac{\langle \Psi_0(r)|V(r)|\Psi_n(r)\rangle^2}{E_n - E_0} \tag{15}$$

According to Eq. (15), a structural instability takes place when the total force constant, K, is negative, thus $K_0 < K_v$. As fluorides have a strong K_0 constant that condition is not fulfilled for a Cu^{2+} impurity, but the orthorhombic instability takes place in the pure compound K_2CuF_4 where two adjacent CuF_6^{4-} units share a common F^-. This cooperative effect favors $K < 0$ such as it is discussed in Ref. [18].

For the sake of clarity, on Figure 4 are displayed the effects of an orthorhombic instability on a CuF_6^{4-} complex which is *initially* tetragonally *compressed* ($R_X = R_Y > R_Z$). If the total force constant, K, for the orthorhombic distortion is negative then the final equilibrium geometry for the CuF_6^{4-} unit is no longer D_{4h} but D_{2h}, thus modifying the distances between F^- ions in the XY plane and Cu^{2+} (Figure 4). That switch also involves a change of the electronic density. Indeed, if under a compressed D_{4h} geometry, the unpaired electron is in a $3z^2$-r^2 molecular orbital, it can be mixed with the x^2-y^2 under the orthorhombic distortion, Q. This produces an increase of the $3z^2$-r^2 energy and a diminution of that for x^2-y^2 (Figure 4). The *different population* of $a_{1g}(3z^2\text{-}r^2)$, $b_{1g}(x^2\text{-}y^2)$ orbitals of the CuF_6^{4-} complex gives rise to a decrement of the electronic energy such as it is shown in Eq. (13).

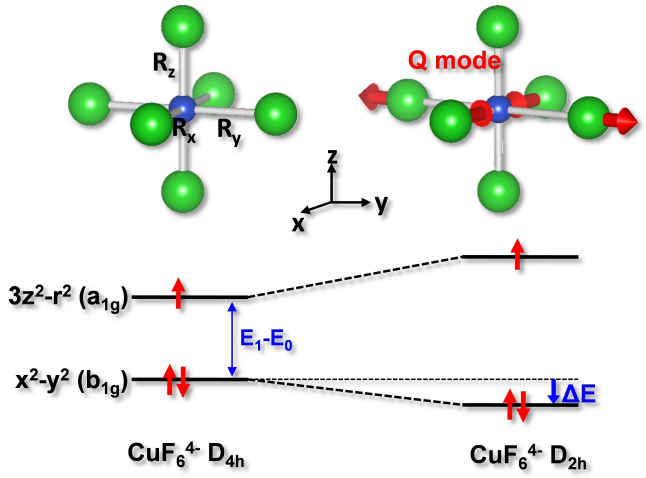

Figure 4. Left: x^2-y^2 and $3z^2$-r^2 levels of a tetragonally (D_{4h}) compressed CuF_6^{4-} complex (with $R_X = R_Y > R_Z$). Right: Effect on the levels of the complex due to the orthorhombic distortion induced by a negative force constant, $K < 0$.

It is worth noting now that the orthorhombic instability of Figure 4 in a tetragonal complex like CuX_6^{4-} (X = halide) is strongly favored when it is compressed rather than elongated.[18,82] Indeed, the distance among the central cation and ligands in the XY plane is higher in a compressed than in an elongated geometry. This fact makes that K_0 is reduced for a compressed configuration as the anharmonicity lowers the force constant of a given bond when its length increases.[8,73] For this reason, the orthorhombic instability is not observed in tetragonally elongated systems like $NaCl:Cu^{2+}$[77], $CsCdF_3:Cu^{2+}$[83] or La_2CuO_4[84]. By contrast, it is developed in copper Tutton salts like $K_2Cu(H_2O)_6(SO_4)_2$ where the internal electric field forces the hole to be in a $3z^2$-r^2 molecular orbital.[85] This in turn favors an initial compressed conformation and a subsequent orthorhombic distortion in the xy plane.

It is important to emphasize that the coupling between states that are separated by an energy gap can happen *regardless the degeneracy of the ground state*, provided the condition $\Gamma_0 \times \Gamma_n \supset \Gamma$ is fulfilled. This stands in contrast to the JT effect, which requires the existence of a degenerate ground state. Consequently, it becomes essential to examine each individual system to determine the predominant coupling mechanism.

Furthermore, recent research[18,78,85] has shown that the mixing of two or more states separated by an energy gap is the driving force behind the structural distortions observed in numerous low-symmetry systems containing transition metal ions. Given that this coupling involves states separated by an energy gap, it is not a first but a *second-order* perturbation effect. This second-order vibronic effect is commonly referred to as the pseudo Jahn-Teller effect (PJT) in the literature.[86] However, it is noteworthy that this term could be misleading, as the JT and PJT are distinct phenomena arising from vibronic interactions. For instance, instabilities caused by the so called PJT effect necessarily involve a negative force constant while in a typical JT effect it is positive.

2.4. Internal Electric Fields in Insulating Compounds

As previously indicated, the concept of MX_N transition metal complex is very useful to explain many properties of insulating materials, an idea based on the fact that active electrons are essentially confined within the MX_N units.[8–11] This description is supported by Magnetic Resonance data and theoretical calculations showing that unpaired electrons are localized within the MX_N complex. For example, calculations carried out on $KMgF_3:Ni^{2+}$ strongly support that valence electrons are essentially localized in the NiF_6^{4-} unit.[87] The results of ENDOR (Electron Nuclear Double Resonance) on $Al_2O_3:Cr^{3+}$, $MgAl_2O_4:Cr^{3+}$ are also consistent with the electron localization inside the CrO_6^{9-} complex.[88,89]

Although the idea of an isolated complex is a good starting point for understanding the properties of insulating compounds with TM cations, there are relevant features that cannot be explained on this ground. Indeed, in insulating solids with a dominant ionic character, complexes are *not isolated but*

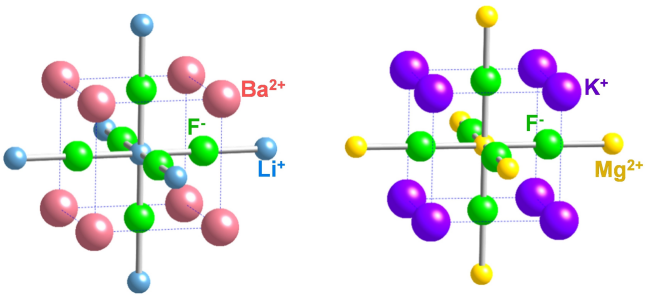

Figure 5. 21 atom clusters used in the calculations of the inverse $BaLiF_3$ (left) and normal $KMgF_3$ (right) perovskite structures. Unit cells are marked with dashed lines. The lattice constant *a* is thus equal to $2R_0$. Similar clusters were used for the calculations of the corresponding Ni^{2+} impurity centers but replacing the central ion (Li^+ in $BaLiF_3$, Mg^{2+} in $KMgF_3$) by Ni^{2+}. Adapted figure with permission from [A. Trueba, J. M. García-Lastra, M. T. Barriuso, J. A. Aramburu, M. Moreno, *Phys. Rev. B: Condens. Matter Mater. Phys.* **2008**, *78*, 075108] Copyright (2023) by the American Physical Society.

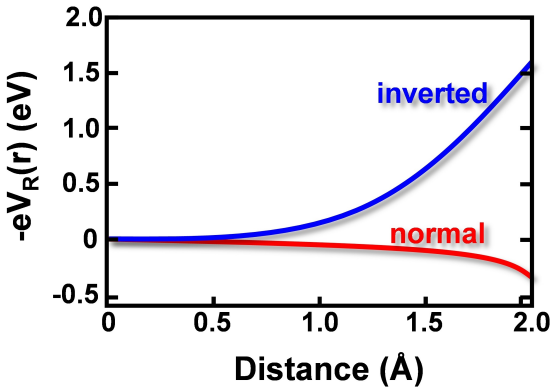

Figure 6. Electrostatic energy, $-eV_R(\mathbf{r})$, describing the interaction between an electron of a NiF_6^{4-} complex of Ni^{2+}-doped the inverted $BaLiF_3$ perovskite and normal $KMgF_3$ perovskite depicted along $<100>$ type directions with the electrostatic potential, V_R, due to the rest of lattice ions.

embedded in a lattice made of ions. Therefore, electrons inside a transition metal complex are subject to the internal electric field, $\mathbf{E}_R$, produced by the rest of lattice ions lying *outside* the complex. It is worth noting that if such ions display spherical symmetry, the net electric field created on the complex would strictly be zero, according to the Gauss theorem in electrostatics. However, this situation cannot in general take place in a real crystal where the symmetry is at most cubic.

Therefore, in general, it is necessary to consider the effects of the internal electric field, $\mathbf{E}_R$, for properly explaining the optical spectrum and the nature of the ground state of TM complexes in insulating compounds. Only in a few systems, like normal perovskites,[8,55,87] the electrostatic potential V_R ($E_R(r) = -\nabla V_R(r)$) is quite flat in the complex region, thus it can be neglected. By contrast, in compounds displaying a layered structure,[15,18,85,90] the internal field often determines the nature of the electronic ground state. Along this line, it is shown in section 3.1 how the electric field due to rest of lattice ions is instrumental in understanding the different optical transitions observed when the same complex CuF_6^{4-} is placed in different lattices.

Another example concerns the different electrostatic potential observed in the normal (Figure 5, right) and inverted (Figure 5, left) perovskites doped with TM cations like Ni^{2+} or Mn^{2+}. These impurities substitute Mg^{2+} and Li^+ in $KMgF_3$ and $BaLiF_3$ respectively, that have nearly identical ionic radius.

The potential energy, $-eV_R$, acting on a single electron along $\langle 100 \rangle$ direction in normal and inverted perovskite is represented in Figure 6. Thus $-eV_R$ is essentially flat for the normal perovskite while it rises the electron energy in the inverted one. As $e_g(3z^2\text{-}r^2, x^2\text{-}y^2)$ electrons mainly lie along $\langle 100 \rangle$ directions $-eV_R$ in $BaLiF_3$ tends to increase the energy of that orbital and also the 10Dq value.

The distinct behavior of V_R in $KMgF_3$ and $BaLiF_3$ can reasonably be understood just considering the first two shells surrounding the complex (Figure 5).[55,87] In $KMgF_3$ the first shell involves a cube of *monovalent* K^+ ions producing an increase of 10Dq, while in the second shell there is an octahedron of *divalent* Mg^{2+} ions yielding a negative contribution to 10Dq that practically cancels the first shell contribution. By contrast, in $BaLiF_3$, the changes in 10Dq due to V_R essentially arise from the first shell that in this case is composed by a cube of *divalent* Ba^{2+} ions thus tending to enhance the 10Dq value. A further discussion on this issue is given in section 4.1.

3. Optical Properties of Insulating Compounds with d^n Ions (n = 4, 9): Influence of Instabilities and Internal Fields

3.1. d–d Transitions due to Cu^{2+} Ions in $KZnF_3$, K_2ZnF_4 and K_2CuF_4

In this section, our primary focus will be on fluorides, as they exhibit favorable characteristics as host lattices for exploring the optical properties of transition metal compounds. Fluorides are harder than other halides with higher ionic radii and besides, they show a wider transparency window in the visible-ultraviolet range, a property intricately linked to the higher electronegativity of fluorine.[91] Here, we examine the experimental and theoretical results on $KZnF_3:Cu^{2+}$, $K_2ZnF_4:Cu^{2+}$, K_2CuF_4 which are rather similar in composition. The structure of pure lattices is described in Refs. [92–95]. Calculations have been performed in the framework of Density Functional Theory.[96] We will first explore the case of a cubic perovskite, namely $KZnF_3$ (Figure 7, left), with a Cu^{2+} impurity replacing a Zn^{2+} ion, thus forming a CuF_6^{4-} complex.[19,25,29,78,79] In the high symmetry parent phase, the CuF_6^{4-} complex exhibits perfect cubic symmetry, therefore a static JT effect can take place, as there is a net force acting on ligands due to the unpaired electron of Cu^{2+}, as explained in section 2.1. When subject to the constraint of octahedral symmetry, the $Zn^{2+} \rightarrow Cu^{2+}$ substitution has minimal impact on the metal-ligand distance, with only a slight increase from 2.00 Å in the pure system to 2.03 Å in the doped system.[25] Upon relaxation of the geometry, the system attains an equilibrium configuration characterized by an elongated octahedron (Figure 2). In this configuration, two of

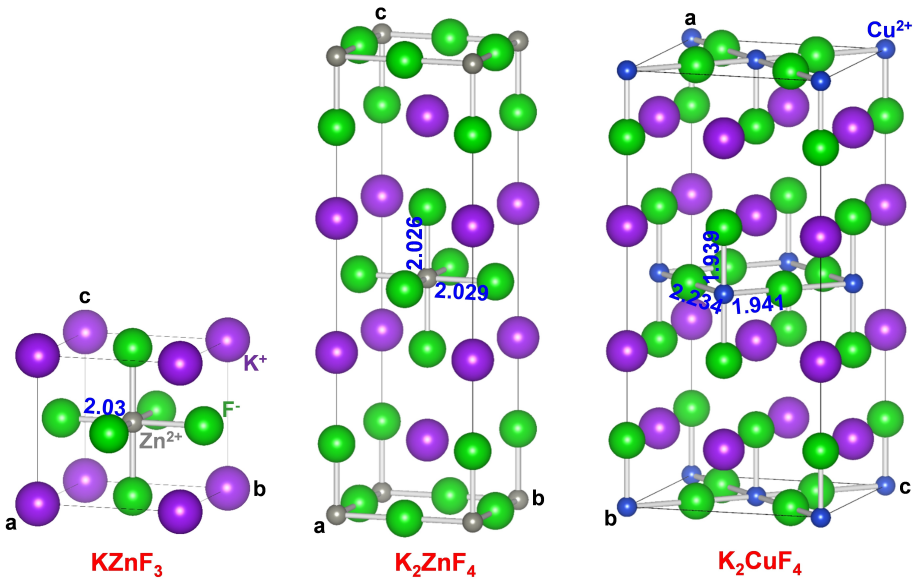

Figure 7. Crystal structures of $KZnF_3$ (cubic perovskite),[92,94] K_2ZnF_4[93,94] and K_2CuF_4[95] (layered perovskites) materials.

the metal-ligand distances, denoted as R_{ax}, increase to 2.102 Å, while the remaining four distances, R_{eq}, shorten to 1.967 Å. The local tetragonal distortion opens a gap, Δ, between the B_{1g} (x^2-y^2) and A_{1g} ($3z^2$-r^2) states, which is unaffected by the internal electric field since the rest of lattice ions keeps cubic symmetry.[25,78,79] According to experimental measurements,[20] this gap will be below 0.5 eV.

We shall now shift our focus towards lattices with lower symmetry, such as K_2ZnF_4:Cu^{2+} (Figure 7, center) and K_2CuF_4 (Figure 7, right). In general, the energy gap Δ between B_{1g} and A_{1g} states has been linked to the local tetragonal distortion of CuF_6^{4-} units, induced by vibronic mechanisms such as the JT effect.[25] However, the mere consideration of local distortions is insufficient to elucidate the differences observed in the optical spectra of the three fluorides. For example, in the tetragonal host lattice K_2ZnF_4 doped with Cu^{2+}, the gap Δ between the B_{1g} and A_{1g} states is negative (as detailed in Table 1),[21,22,25] in contrast to what is found for the cubic host lattice $KZnF_3$. Accordingly, the ground state of CuF_6^{4-} complex embedded in the K_2ZnF_4 lattice is A_{1g}. This change in the electronic configuration corresponds to a slightly compressed octahedral geometry.

Table 1 shows the equilibrium metal-ligand distances and energy gaps Δ for the three copper fluorides obtained by means of first principles calculations. The gap Δ has been calculated for isolated CuF_6^{4-} complex, also considering the electric field created by the rest of lattice ions. The data collected on distances and gaps are consistent with experimental observations.

Based on the values gathered in Table 1, the local geometry of the CuF_6^{4-} complex in the cubic lattice $KZnF_3$ is tetragonally elongated, whereas it is compressed in the tetragonal lattice K_2ZnF_4. Moreover, the electrostatic potential created by the rest of lattice ions in $KZnF_3$ leads to shifts in Δ practically negligible, while in the tetragonal system the shift is around 0.3 eV.[25,78]

It is noteworthy that all d–d transition energies, schematically displayed in Figure 8, show a shift towards higher energies in K_2ZnF_4:Cu^{2+} compared to $KZnF_3$:Cu^{2+}, a fact that cannot be entirely explained in terms of the local geometry. The key difference between these two systems is the *internal electric field* (section 2.4), which plays a significant role in layered compounds such as K_2ZnF_4.[15,18,22] In the case of $KZnF_3$, the internal electric field exhibits cubic symmetry, thus the three directions of the CuF_6^{4-} complex are equivalent in the initial

Table 1. Calculated equilibrium axial (R_{ax}), and equatorial short (R_{eq}^{s}) and long (R_{eq}^{l}) metal-ligand distances (in Å) for the CuF_6^{4-} complex embedded in different fluorine lattices.[25,78] Energy gap, Δ (in eV), between B_{1g}(x^2-y^2) and A_{1g}($3z^2$-r^2) states for an isolated complex and also considering the internal potential V_R due to the rest of the lattice ions.[25,78] Positive/negative values of Δ correspond to a dominant B_{1g}/A_{1g} ground state. For comparison, the experimental value of Δ and Cu–F distances measured in K_2CuF_4 (second row, in italics) are also collected.[24,95] R_0 (in Å) denotes the experimental values of metal-ligand distances for $KZnF_3$[92,94] and K_2ZnF_4[93,94] pure systems.

System	R_0	R_{ax}	R_{eq}^{s}	R_{eq}^{l}	Δ (isolated) calculated	Δ ($+V_R$) calculated	Δ experim.
$KZnF_3$:Cu^{2+}	2.03	2.102	1.967	1.967	0.36	0.40	*< 0.5*
K_2ZnF_4:Cu^{2+}	2.02	1.931	2.041	2.041	−0.33	−0.61	≈ −0.7
K_2CuF_4	–	1.937 *1.939*	1.900 *1.941*	2.223 *2.234*	−0.76	−1.01	−1.03

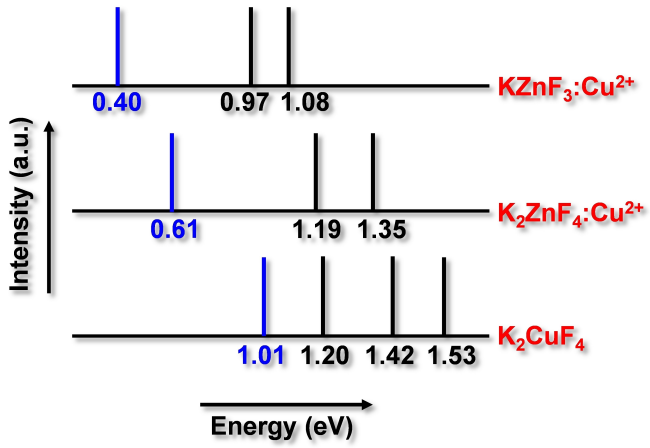

Figure 8. Calculated values of the absolute d–d transition energies (in eV) for $KZnF_3:Cu^{2+}$, $K_2ZnF_4:Cu^{2+}$ and K_2CuF_4. Blue lines correspond to the first transition $B_{1g}(x^2\text{-}y^2)\rightarrow A_{1g}(3z^2\text{-}r^2)$ for $KZnF_3:Cu^{2+}$ while $A_{1g}(3z^2\text{-}r^2)\rightarrow B_{1g}(x^2\text{-}y^2)$ for $K_2ZnF_4:Cu^{2+}$. The ground state for the CuF_6^{4-} complex in K_2CuF_4 has a dominant $A_g(3z^2\text{-}r^2)$ character.

situation, i.e., in the octahedral configuration. Conversely, in K_2ZnF_4, the electric field displays notable differences between the axial and the equatorial directions.

The associated electrostatic potentials are depicted in Figure 9, clearly demonstrating that the tetragonal electrostatic potential of K_2ZnF_4 introduces an energy gap between $x^2\text{-}y^2$ and

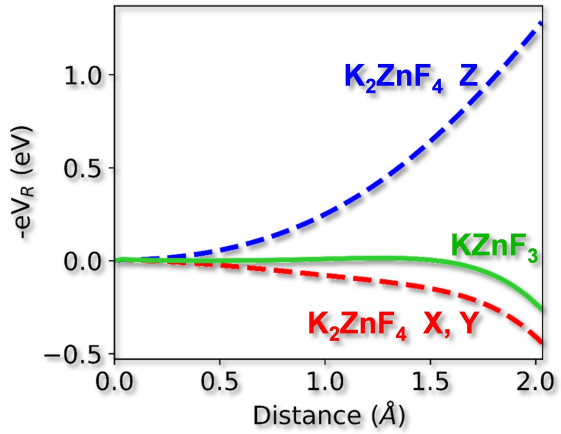

Figure 9. Electrostatic energy $-eV_R(\mathbf{r})$ between an electron in a CuF_6^{4-} complex and the rest of lattice ions in Cu^{2+}-doped $KZnF_3$ cubic lattice along any $<100>$ direction (green curve), compared to the ones for a CuF_6^{4-}-complex in K_2ZnF_4 tetragonal lattice displayed along X, Y (red dotted curve) and Z (blue dotted curve) directions.

Table 2. Calculated and experimental energies (in eV) of d–d transitions for a CuF_6^{4-} complex at its equilibrium geometry in $K_2ZnF_4:Cu^{2+}$. Calculated values for the isolated CuF_6^{4-} complex as well as considering the electrostatic potential V_R of the rest of the lattice ions are included.[25,78]

Transition	Isolated	$+V_R$	Experimental
A_{1g} $(3z^2\text{-}r^2)\rightarrow B_{1g}(x^2\text{-}y^2)$	0.33	0.61	~0.70
A_{1g} $(3z^2\text{-}r^2)\rightarrow E_g$ (xz, yz)	1.08	1.19	~1.15
A_{1g} $(3z^2\text{-}r^2)\rightarrow B_{2g}$ (xy)	1.17	1.35	1.33

$3z^2\text{-}r^2$ orbitals, even when the ligands are at the same distance.[15,18,22] Consequently, the existence of a JT effect is excluded. From Figure 9, it can be inferred that the most energetically favorable state in K_2ZnF_4 is achieved by placing the unpaired electron in the $3z^2\text{-}r^2$ orbital.

According to Table 2, the energies of d–d transitions in $K_2ZnF_4:Cu^{2+}$, corresponding to the excitation of a hole from $3z^2\text{-}r^2$ to the other d orbitals, cannot be understood without considering the influence of the internal electric field.

Finally, if we move forward from doped $K_2ZnF_4:Cu^{2+}$ to pure K_2CuF_4, two key factors govern the local geometry and the ground state of CuF_6^{4-} complex. Firstly, as previously discussed, the internal electric field favors the localization of the unpaired electron in the $3z^2\text{-}r^2$ orbital. Secondly, in the pure K_2CuF_4 compound, an *additional orthorhombic distortion* appears in the layer plane, as evidenced by the data compiled in Table 1. This orthorhombic distortion results in the shortening of two metal-ligand distances in the layer plane, thus reinforcing these bonds, while elongating the other two (Figure 7, right). By contrast, the axial distance is barely affected, as it is practically the same in $K_2ZnF_4:Cu^{2+}$ (1.931 Å), in K_2CuF_4 (1.939 Å). Although the orthorhombic distortion conveys a hybridization of $3z^2\text{-}r^2$ and $x^2\text{-}y^2$, the unpaired electron retains a dominant $3z^2\text{-}r^2$ character (around 80%)[18,80] in agreement with available EPR data.[23] This instability, observed in several low symmetry pure compounds, is enhanced by the cooperative in-plane distortion of the CuF_6^{4-} centers, which share a common ligand such as it happens in the K_2CuF_4 lattice.[18] By contrast, in $KAlCuF_6$, the CuF_6^{4-} units are well separated and the orthorhombic distortion is absent.[35,36,39] The lack of this enhancement due to a cooperative effect is also behind the absence of the orthorhombic distortion in $K_2ZnF_4:Cu^{2+}$ thus implying a positive force constant, K, for such a mode.[18,22,25] Nevertheless, if K_0 is reduced, replacing F by Cl as ligands, the orthorhombic distortion can be observed for a single impurity such as it happens for $(C_2H_5NH_3)_2CdCl_4:Cu^{2+}$,[18,43] a matter discussed in section 3.3.

The underlying mechanism driving the observed orthorhombic distortion is discussed in section 2.3. That instability is associated with an orthorhombic b_{1g} mode, characterized by a negative force constant (Eq. (14)). Consequently, the system evolves to the orthorhombic configuration that minimizes the overall energy. This distortion contributes to increase the energy gap Δ when transitioning from the Cu^{2+}-doped K_2ZnF_4 to K_2CuF_4 such as it is shown in Table 1, Figure 8.

3.2. Absorption Spectrum of CrF_2 and CuF_2 Compounds

In this section, our focus will be on two compounds, CrF_2 (containing the d^4 Cr^{2+} ion) and CuF_2 (involving the d^9 Cu^{2+} ion), usually considered as textbook examples of distorted CrF_6^{4-} and CuF_6^{4-} complexes due to a $E_g\otimes e_g$ JT effect.[27–30,33,97] However, it has recently been shown[31,34] that the distortion mechanism bears similarities to that observed in K_2CuF_4. This discovery allows one to gain insights into the actual origin of

experimental d–d optical bands observed in both CrF_2 and CuF_2 materials.[29,33]

Both compounds exhibit a low symmetry monoclinic structure which is usually described by the non-standard $P2_1/n$ space group (Figure 10, left, Table 3; the standard group is $P2_1/c$). In the usual view, CrF_6^{4-}, CuF_6^{4-} complexes are considered to have an elongated quasi-D_{4h} local geometry induced by a $E_g \otimes e_g$ JT effect from a high symmetry ZnF_2 parent phase (rutile structure, $P4_2/mnm$ space group; see Figure 10, right) where the ZnF_6^{4-} complexes are considered as quasi-octahedral. Following this usual interpretation, CrF_6^{4-} or CuF_6^{4-} complexes in the $P4_2/mnm$ parent phase would have a E_g degenerate ground state and so they could be subject of a JT effect.[27–30,33,97]

However, an appropriate analysis of the experimental structures of these compounds casts doubts on this interpretation. On one hand, the ZnF_2 parent phase contains ZnF_6^{4-} complexes with orthorhombic D_{2h} symmetry, with two different Zn–F distances, $R_X = R_Y = 2.040$ Å, $R_Z = 2.019$ Å, the angle between X, Y axes significantly deviates from 90° ($\phi = 79.7°$, Table 3).[98] On the other hand, the CrF_6^{4-} complexes in the final monoclinic $P2_1/n$ structure of CrF_2 (similar in CuF_2) have a monoclinic C_{2h} symmetry with $R_X = 2.011$ Å, $R_Y = 2.478$ Å, $R_Z = 1.978$ Å, $\phi = 76.1°$, a final geometry not compatible with a $E_g \otimes e_g$ JT effect.

Due to the similarity between CrF_2 and CuF_2 the present analysis is henceforth mainly focused on CrF_2. First principles calculations carried out on CrF_2[34] have shown the importance of considering the true symmetry of the complexes in order to understand the structure and optical d–d spectrum of this system. Calculations were performed in 4 steps:

(1) Obtaining the parent phase of the monoclinic $P2_1/n$ structure of CrF_2. In this step, all open-shell Cr^{2+} ions were substituted by closed-shell Zn^{2+} ones and, optimizing this ZnF_2 lattice fixing the $P2_1/n$ space group. Interestingly, this process leads to the experimental tetragonal $P4_2/mnm$ structure of ZnF_2, with ZnF_6^{4-} complexes of orthorhombic D_{2h} symmetry with geometry $R_X = R_Y = 2.043$ Å, $R_Z = 2.009$ Å, $\phi = 79.5°$, in excellent agreement with the experimental data in Table 3.

(2) Maintaining fixed the $P4_2/mnm$ group, all Zn^{2+} ions were substituted by Cr^{2+} ones reoptimizing the structure, obtaining orthorhombic D_{2h} CrF_6^{4-} complexes with $R_X = R_Y = 2.170$ Å, $R_Z = 1.962$ Å, $\phi = 79.4°$.

(3) A single point calculation was performed on a D_{2h} CrF_6^{4-} complex at the optimized geometry in the $P4_2/mnm$ parent phase. The corresponding ground state involves a hole placed in an orbital with mainly $3z^2$-r^2 character due to the compressed geometry of the complex, also the effect of the electrostatic field of the lattice, which differs along the axial (Z), equatorial (X, Y) directions, favoring the occupation of the mainly x^2-y^2 orbital. As the complex involves a ϕ angle different of 90°, there is a small hybridization of x^2-y^2, $3z^2$-r^2 orbitals.

(4) Calculation of harmonic vibration frequencies at the optimized geometry of the $P4_2/mnm$ parent phase of CrF_2. That study shows that for a given CrF_6^{4-} complex there is

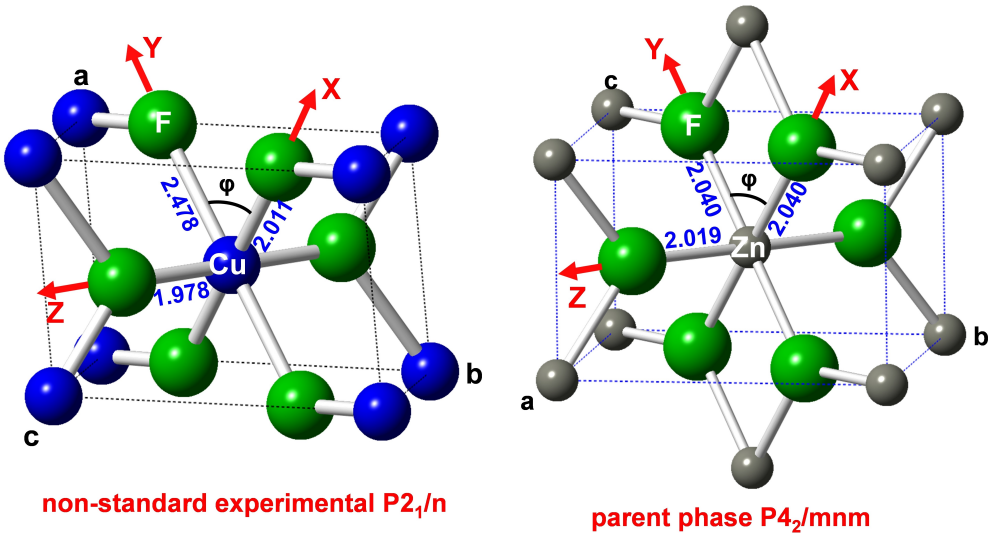

Figure 10. Left: Monoclinic structure of CrF_2[32], CuF_2[27,30] materials described by the non-standard $P2_1/n$ space group (the standard group is $P2_1/c$). Right: Tetragonal $P4_2/mnm$ (rutile ZnF_2 type) parent phase of CrF_2, CuF_2.

Table 3. Experimental lattice parameters a, b, c (in Å), β angle (in degrees) and metal-ligand distances (in Å) of tetragonal $P4_2/mnm$ ZnF_2[98] and monoclinic standard $P2_1/c$ CrF_2[32], CuF_2.[27,30] The angle ϕ (in degrees) formed by X and Y local axes is also detailed.

System	a	b	c	β	R_X	R_Y	R_Z	ϕ
ZnF_2	4.704	4.704	3.133	90	2.040	2.040	2.019	79.7
CrF_2	4.732	4.718	6.200	145.8	2.011	2.427	1.978	76.1
CuF_2	3.294	4.568	5.358	121.2	1.932	2.298	1.917	78.1

an *imaginary* frequency associated with a symmetry lowering where the equatorial distances are no longer equivalent, with $R_Y > R_X$ in the experimental $P2_1/c$ phase.

It is worth highlighting that, analogous to $K_2ZnF_4:Cu^{2+}$, the tetragonal to monoclinic transition is not observed in diluted impurities of Cu^{2+} in the pure ZnF_2 material.[99] The cooperative distortion arising from adjacent complexes that share a common ligand results in a negative force constant which leads to the observed distortion of the system.[18,34] Ab initio calculations have shown that, even after orthorhombic distortion, the hole again maintains a strong $3z^2$-r^2 character.[34] It should be emphasized that the presence of this orthorhombic distortion is particularly favored when the hole occupies a $3z^2$-r^2 orbital.

Given the findings concerning the structure and ground state of CrF_2, we are now in conditions to explore the experimental absorption spectrum of this system.[33] Table 4 shows the calculated energies associated with d–d- transitions in CrF_2 for both parent $P4_2/mnm$ phase and experimental $P2_1/c$ phase. Corresponding experimental transitions are also documented in Table 4.

The results presented in Table 4 indicate that the first d–d transition experiences the most significant change during the transformation from the tetragonal $P4_2/mnm$ to the monoclinic $P2_1/c$ phase. Moreover, calculations have shown[31,34] that the electric field has a minimal effect on the transition energy, resulting in a slight increase of only 0.04 eV. This contrasts with layered compounds like K_2CuF_4, where the inclusion of the internal electric field is crucial for understanding the optical d–d spectrum, as discussed in the previous section. Conversely, the orthorhombic distortion of the complexes contributes to a notable increase in energy by 0.63 eV.

The orthorhombic instability also plays a crucial role in understanding the significantly higher measured value of the lowest d–d optical transition[33] in CrF_2, $E = 1.23$ eV, compared to a JT system like $KZnF_3:Cu^{2+}$, where $E = 0.4$ eV, as discussed in section 3.1. This high transition energy is also observed in the analogous copper compound, CuF_2, where $E = 0.93$ eV.[29]

It is important to note that, despite the local orthorhombic D_{2h} symmetry of the CrF_6^{4-} complexes in the $P4_2/mnm$ parent phase, they can approximately be considered as quasi-tetragonal D_{4h}, thus the hole is localized in a mainly $a_{1g}(3z^2$-$r^2)$ orbital with very small hybridization with $b_{1g}(x^2$-$y^2)$. However, after the monoclinic distortion the local symmetry of the complexes is reduced from D_{2h} to C_{2h} and orbitals $3z^2$-r^2 and x^2-y^2 considerably hybridize, although the hole preserves a dominant $3z^2$-r^2 character.[34] This hybridization tends to increase the electronic density along the X local direction when $R_Y > R_X$, and R_X becomes closer to R_Z. This led to the mistaken assumption of a JT effect with elongated tetragonal complexes along Y direction in CrF_2 and CuF_2.[27–30,33,97] However, after careful consideration it becomes evident that there is not a solely elongation along Y direction, but rather a more complex interplay between the axes as consequence of monoclinic distortion.[31,34] The changes in local symmetry, hybridization of orbitals due to this distortion lead to significant alterations of electronic states and transition energies. This highlights the critical role played by the distortion in understanding the optical properties.

Table 4. Calculated d–d transition energies (in eV) in a CrF_6^{4-} complex of CrF_2 at two different geometries:[34] that corresponding to the $P4_2/mnm$ parent phase ($R_X = R_Y = 2.17$ Å, $R_Z = 1.962$ Å) and that in the final $P2_1/n$ phase ($R_X = 2.011$ Å, $R_Y = 2.427$ Å, $R_Z = 1.978$ Å). Experimental values in the $P2_1/n$ phase are also included.[33]

Transition	Calculated $P4_2/mnm$	Calculated $P2_1/n$	Experimental
x^2-$y^2 \rightarrow 3z^2$-r^2	0.60	1.23	1.22
$xz \rightarrow 3z^2$-r^2	1.26	1.35	1.36
$yz \rightarrow 3z^2$-r^2	1.26	1.61	1.75
$xy \rightarrow 3z^2$-r^2	1.50	1.58	1.75

3.3. Optical Excitations in Layered Organic-inorganic Chloroperovskites with Cu^{2+}

In recent years, there has been a significant surge of interest in hybrid organic-inorganic compounds. These materials have attracted attention due to their ability to combine the electronic properties of the inorganic component with the structural versatility offered by organic complexes. This combination of characteristics grants these materials exceptional functionality, making them highly promising for a wide range of novel applications. Particularly, their potential in the development of advanced optical devices and optoelectronics has positioned them as compelling candidates for technological applications in this field.[5–7]

Many hybrid materials exhibit layered structures, where the inorganic components form distinct slabs that are separated by organic elements. For instance, organic-inorganic perovskites such as those found in the $(C_nH_{2n+1}NH_3)CuCl_4$[40,100–103] or $[NH_3(CH_2)_nNH_3]CuX_4$ (X=Cl, Br)[42,104] families exemplify this arrangement. As a salient feature, in these layered materials containing $CuCl_6^{4-}$ units displaying a local orthorhombic symmetry, certain optical transitions can undergo a red shift instead of the blue shift when subject to pressure.[6,41,43] This situation is, in principle, puzzling in view of optical data for high symmetry complexes. For instance, in *octahedral* TM complexes, the energy gap between e_g, t_{2g} electronic levels, known as 10Dq parameter (Figure 1), depends on the metal-ligand distance, R, as[8,105]

$$10Dq = CR^{-n} \tag{16}$$

where C is a constant, the exponent *n* falls in the approximate range 4–6.

This high sensitivity of 10Dq to R variations is the result of the different chemical bonding involved in the antibonding e_g, t_{2g} orbitals.[11,8,105] Thus, in accord with Eq. (16) an increase of pressure tends to enhance the gap between such orbitals. In the same vein, the charge transfer transitions of a simple square-planar $CuCl_4^{2-}$ complex also undergo a blue shift when the Cu–Cl distance, R, is reduced by a hydrostatic or chemical pressure.[106–109] This fact mainly reflects the energy increase

experienced by mainly 3d orbitals of copper when the negatively charged ligands are approached.[8]

As discussed in previous sections, there is a *correlation* between optical properties and structure. Hence, the observed red shift under pressure can be attributed to the non-equivalence of all the involved ligands related to the local orthorhombic geometry. As it is discussed below, this fact emphasizes the influence of structural factors on the resulting optical behavior. The non-equivalency of ligands has been confirmed through first principles calculations on $(C_2H_5NH_3)_2CdCl_4:Cu^{2+}$.[43]

The optimized structure of $(C_2H_5NH_3)_2CdCl_4:Cu^{2+}$, which serves as a model system of these copper-layered hybrid compounds, is depicted in Figure 11. The metal-ligand distances at zero pressure for this compound, as well as other pure, Cu^{2+}-doped compounds of $(C_nH_{2n+1}NH_3)_2CuCl_4$ family, are detailed in Table 5. These data show that the local geometry of $CuCl_6^{4-}$ complexes exhibits an orthorhombic arrangement, with the longest axis lying along the Y local direction.

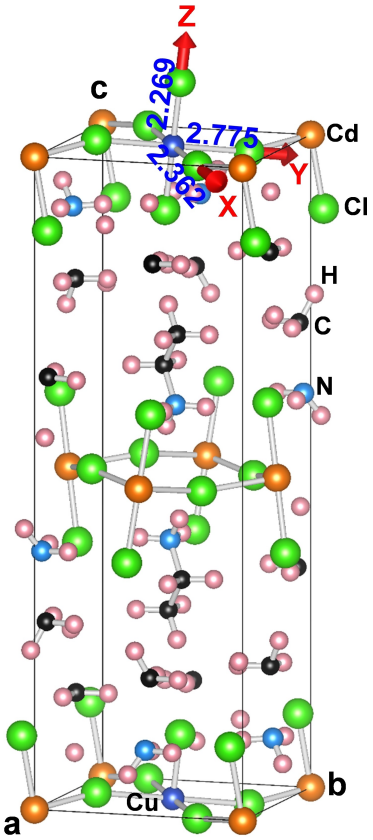

Figure 11. Optimized structure of $(C_2H_5NH_3)_2CdCl_4:Cu^{2+}$. The Z axis is perpendicular to the layer plane while X and Y axes are lying in the layer plane.

For understanding the local structure around Cu^{2+} in $(C_2H_5NH_3)_2CdCl_4:Cu^{2+}$, it is necessary to consider what happens in the pure compound[110] $(C_2H_5NH_3)_2CdCl_4$ as Cu^{2+} substitutes Cd^{2+}. As shown on Table 5, the local geometry around Cd^{2+} in the pure compound is tetragonally compressed with a main axis along Z (Figure 11), Cd^{2+}–Cl^- distances given by $R_X = R_Y = 2.673$ Å and $R_Z = 2.522$ Å (Table 5). The final geometry derived for $CuCl_6^{4-}$ in $(C_2H_5NH_3)_2CdCl_4:Cu^{2+}$ is again the result of an orthorhombic instability helped by an initial compressed configuration such as it has been discussed in section 2.3. It is worth noting that such instability can appear more easily for Cu^{2+} *impurities* in chlorides than in fluorides as K_0 is usually higher in the second case. Supporting this view, that instability is experimentally observed[18,41,43] for $(C_2H_5NH_3)_2CdCl_4:Cu^{2+}$ and $(CH_3NH_3)_2CdCl_4:Cu^{2+}$ but not for $K_2ZnF_4:Cu^{2+}$, such it is shown in section 3.1. It is worth noting that in cases like $(CH_3NH_3)_2CdCl_4:Cu^{2+}$ the orthorhombic instability implies the existence of two equivalent situations. A dynamical process involving incoherent jumps between both situations is well observed in EPR spectra upon raising the temperature.[18]

Interestingly, the data collected in Table 5 indicate that the longest R_Y distance tends to increase as the size of organic molecules increases. This observation implies that the bond associated with the longest R_Y distance is particularly sensitive to changes in the compound's composition, thus suggesting that such a bond is much softer than those along X or Z directions.

This central idea is underpinned by results of calculations on $(C_2H_5NH_3)_2CdCl_4:Cu^{2+}$ under pressure.[43] For instance, the calculations yield that under a pressure of only 3 GPa, the R_Y distance is reduced in 0.21 Å whereas R_X, R_Z remain practically unmodified. Moreover, such calculations reveal that the force constant associated with the long bond along Y axis is remarkably small $K_Y = 1.1$ eV/Å^2. Indeed, in $NaCl:Cu^{2+}$, where the $CuCl_6^{4-}$ complex is elongated due to the Jahn-Teller effect, the calculated force constant for moving the soft axial ligand is practically three times bigger.[43] These results provide quantita-

Table 5. Experimental values of the equatorial R_X, R_Y and axial R_Z distances (in Å) for three pure $(C_nH_{2n+1}NH_3)_2CuCl_4$ compounds and calculated values (determined through first principles calculations with VASP code) for two Cu^{2+}-doped $(C_nH_{2n+1}NH_3)_2CdCl_4$ systems. The structure of the parent $(C_2H_5NH_3)_2CdCl_4$ compound is included for comparison. All values correspond to zero-pressure.

System	R_X	R_Y	R_Z	Refs.
$(C_2H_5NH_3)_2CdCl_4$	2.673	2.673	2.522	[110]
$(CH_3NH_3)_2CdCl_4:Cu^{2+}$	2.441	2.690	2.279	[18]
$(C_2H_5NH_3)_2CdCl_4:Cu^{2+}$	2.362	2.775	2.269	[43]
$(CH_3NH_3)_2CuCl_4$	2.283	2.907	2.297	[100]
$(C_2H_5NH_3)_2CuCl_4$	2.285	2.975	2.277	[40]
$(C_3H_7NH_3)_2CuCl_4$	2.29	3.04	2.29	[101]

tive evidence of the distinct elastic behavior of the bonds and underscore the sensitivity of R_Y to hydrostatic pressure.

As previously mentioned, the nature of the complex ground state is influenced by both the internal electric field, $\mathbf{E}_R$, and the orthorhombic distortion. Calculations have shown[43] that the HOMO wavefunction predominantly exhibits a $3z^2$-r^2 character, accounting for approximately 81% of the electron density. These outcomes are consistent with a tetragonal geometry of the parent phase. However, if the HOMO wavefunction is expressed in the $\{|3y^2-r^2\rangle, |x^2-z^2\rangle\}$ basis, the unpaired electron is predominantly localized (99%) in an orbital with x^2-z^2 character, highlighting the strong localization of the electron density within the XZ plane. In the same way the orbital with a dominant x^2-y^2 character, lying below the HOMO is essentially represented by $3y^2$-r^2 in the $\{|3y^2-r^2\rangle, |x^2-z^2\rangle\}$ basis.

Once we have clarified the origin of local geometry and ground state of $(C_2H_5NH_3)_2CdCl_4$:Cu^{2+} model system, we are able to explore its optical transitions. The calculated d–d transition energies at zero pressure, under 3 GPa are gathered in Figure 12, providing evidence for the remarkable sensitivity of the first d–d $|3y^2-r^2\rangle \rightarrow |x^2-z^2\rangle$ transition to pressure.[43] Indeed, under a pressure of only 3 GPa, this transition experiences an important red shift of 0.34 eV. Conversely, the three d–d transitions coming from the xz, yz, xy orbitals exhibit minimal blue shifts. This different behavior displayed by the d–d transitions can be attributed to the highly anisotropic response of the lattice to pressure. In fact, as discussed above, in the 0–3 GPa range the R_Y local distance is reduced by a significant quantity of 0.21 Å, while R_X and R_Z are essentially unmodified. As a result, the orbital energy of $|3y^2-r^2\rangle$ is the most affected by the applied pressure. Accordingly, its energy strongly increases with pressure thus leading to a red shift of the $|3y^2-r^2\rangle \rightarrow |x^2-z^2\rangle$ transition energy (Figure 12).

As demonstrated in previous research,[18,43] these results align with experimental and calculated d–d transitions in other hybrid layered compounds. For instance, the experimental energy of the first d–d transition at zero pressure in the pure $(CH_3NH_3)_2CuCl_4$ compound,[111] with a R_Y value of 2.907 Å (Table 5), increases to 1.34 eV in comparison with the value (0.93 eV) derived for $(C_2H_5NH_3)_2CdCl_4$:Cu^{2+}. Similarly, in the case of $(C_2H_5NH_3)_2CuCl_4$ with $R_Y = 2.975$ Å (Table 5) such a transition rises up to 1.38 eV.[112]

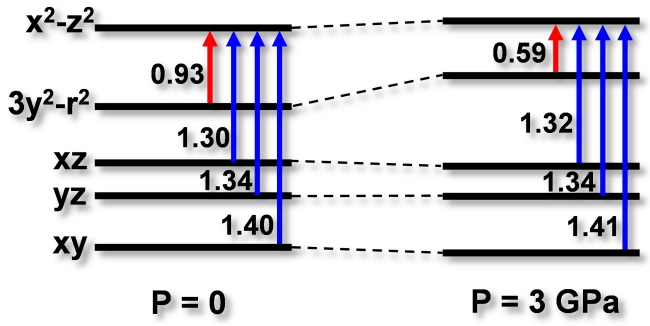

Figure 12. Scheme showing the transition energies (eV) calculated at zero pressure ($R_X = 2.362$ Å, $R_Y = 2.775$ Å, $R_Z = 2.269$ Å geometry) and P = 3 GPa ($R_X = 2.353$ Å, $R_Y = 2.564$ Å, $R_Z = 2.264$ Å) for the $(C_2H_5NH_3)_2CdCl_4$:Cu^{2+} model system.[43] The five involved orbitals are described by the main contribution to the wavefunction. In the ground state of the d^9 complex the unpaired electron is in $|x^2-z^2\rangle$.

4. Optical Properties of Insulating d^3, d^5 and d^9 Transition Metal Compounds not Involving Instabilities: Role of Internal Electric Fields

In this section, we explore the optical properties of d^3, d^5 and d^9 transition metal compounds where the final structure is not a consequence of vibronic instabilities. We will discuss three insightful model systems found in nature. By focusing on these examples, we aim to gain insights into the microscopic origin of the optical behavior exhibited by such compounds, contributing to our overall understanding of their optical properties. Notably, a shared characteristic among these three examples is that their properties cannot be fully understood without considering the influence of the internal electric field, $E_R(\mathbf{r})$, created by the rest of lattice ions, on the active electrons localized in the TM complex.

4.1. Mn^{2+} in Normal and Inverted Perovskites: Understanding the Different Absorption Spectra

As mentioned in section 2.4, the normal and inverted perovskites serve as excellent examples that highlight the importance of the electrostatic potential, $V_R(\mathbf{r})$, when investigating the optical properties of transition metal compounds embedded in insulating lattices.[55,87]

An example of the inverted perovskite structure is $BaLiF_3$ (Figure 5, left), which exhibits a primitive cubic lattice (Pm-3 m space group).[94,113] In this structure, the monovalent Li^+ ions are surrounded by six F^- ions, displaying an octahedral configuration. In contrast, in normal perovskites such as $KMgF_3$ (Figure 5, right), the divalent Mg^{2+} ions are those encompassed by F^- anions.

When $BaLiF_3$ is doped with a 3d cation such as Mn^{2+} or Ni^{2+}, EPR and ENDOR measurements have confirmed that it occupies the Li^+ site with a remote defect for charge compensation.[53,114] Additionally, Extended X-ray Absorption Fine Structure (EXAFS) results obtained from Ni^{2+}-doped $BaLiF_3$ further support these observations.[115]

Despite the structural differences between normal and inverted perovskites, their lattice parameters exhibit remarkable similarity. Indeed, $a = 3.986$ Å and $a = 3.996$ Å for $KMgF_3$ and $LiBaF_3$, respectively. Besides, in the case of Mn^{2+}-doped systems, the local geometry of a MnF_6^{4-} unit remains nearly identical in the two host lattices, with negligible differences[55] between metal-ligand distances, as presented in Table 6. However, an important difference arises in the cubic field splitting, which shows a variation of 0.17 eV between the normal and the inverted perovskite lattices.[52,54,55] Similar observations are derived for Ni^{2+}-doped systems.[87]

In traditional ligand field theory (LFT), the electronic properties of a cubic insulator upon introducing a 3d impurity M are

Table 6. Calculated metal-ligand distances (in Å), R, of Mn^{2+} and Ni^{2+}-doped $KMgF_3$ and $BaLiF_3$ perovskites,[55,87] along with calculated and experimental[54,114] cubic field splitting parameter, 10Dq (in eV).

System	R calculated	10Dq calculated	10Dq experim.
$KMgF_3:Mn^{2+}$	2.063	1.19	1.05
$LiBaF_3:Mn^{2+}$	2.065	1.36	1.22
$KMgF_3:Ni^{2+}$	2.026	1.08	0.97
$LiBaF_3:Ni^{2+}$	2.011	1.29	1.04

explained based *only* on the nature of the impurity and ligands, the coordination number, and the local geometry of the MX_N complexes.[9,10] Consequently, when the same complex is embedded in two different lattices, the changes in electronic and optical properties are attributed to variations of metal-ligand distance, R. This statement is fulfilled in normal fluoroperovskites doped with Mn^{2+}, Ni^{2+} and Cr^{3+} impurities,[105,116,117] where, as stated in Eq. (16), the dependence of cubic field splitting parameter on the metal-ligand distance, R, can be expressed as $10Dq < C{=}CR^{-n}$ with C a constant and n in the range 4–6.[8] However, this theory fails to explain the different 10Dq values for impurities such as Mn^{2+} and Ni^{2+} when the host lattice changes from the normal $KMgF_3$ to the inverted perovskite $BaLiF_3$. In fact, the variation in 10Dq from 1.05 eV[52] in $KMgF_3:Mn^{2+}$ to 1.22 eV in $BaLiF_3:Mn^{2+}$[54,55] cannot be explained on the basis of different metal-ligand distances as the calculated R values for both systems are essentially coincident (Table 6). Additionally, previous studies[55] have shown that the exponents, *n*, obtained for $KMgF_3:Mn^{2+}$ and $LiBaF_3:Mn^{2+}$ are very similar, with $n = 4.62$ for the former, 4.46 for the later.

On the other hand, it has been pointed out in the introduction that LFT falls short in explaining the electronic properties of the same impurity within two non-isomorphous lattices, even if the ligands, the coordination number and the metal-ligand distance are the same. The failure of LFT arises from considering only the *isolated* complexes, thus neglecting the influence of the electric field, $E_R(\mathbf{r})$, generated by the surrounding lattice ions on the electrons within the MX_N complex. This crucial aspect is not considered in classical LFT.

Figure 13 shows the electrostatic potential $V_R(\mathbf{r})$ associated with the internal field $E_R(\mathbf{r})$ along the two ⟨100⟩ and ⟨110⟩ directions for both $KMgF_3$ and $BaLiF_3$ lattices. Along the ⟨100⟩ direction, the energy $-eV_R(\mathbf{r})$ increases significantly in the $LiBaF_3$ lattice, while remaining relatively constant in $KMgF_3$. This observation holds particular significance for the $e_g(3z^2\text{-}r^2, x^2\text{-}y^2)$ orbital, as most of its electronic density is localized along ⟨100⟩ type directions. Therefore, the electrostatic potential tends to increase the energy of this level in $LiBaF_3$ in comparison to $KMgF_3$. In contrast, the impact of $V_R(\mathbf{r})$ is much smaller in t_{2g} (xy, xz, yz) orbitals, which primarily extends along the ⟨110⟩ type directions. This different behavior provides a qualitative explanation for the higher value of 10Dq observed in $LiBaF_3:Mn^{2+}$.

According to the present discussion the cubic field splitting parameter, 10Dq, has, in general, two contributions[49,55]

$$10Dq = (10Dq)_{int} + (10Dq)_{ext} \tag{17}$$

The intrinsic $(10Dq)_{int}$ contribution arises from the effects within the *isolated* complex, while the extrinsic $(10Dq)_{ext}$ contribution accounts for the influence exerted by the electrostatic potential, $V_R(\mathbf{r})$, due to all ions lying outside the MX_N complex, on the localized electrons. Usually $(10Dq)_{ext} \ll (10Dq)_{int}$, thus the extrinsic contribution can be understood as a pertubation with respect to the intrinsic one.[48]

For instance, considering the shape of $-eV_R(\mathbf{r})$ (Figure 13) and the calculated 10Dq values collected in Table 6, the intrinsic contribution for both $KMgF_3:Mn^{2+}$ and $LiBaF_3:Mn^{2+}$ would be $(10Dq)_{int} = 1.05$ eV, while the extrinsic contribution for $LiBaF_3:Mn^{2+}$ amounts to $(10Dq)_{ext} = 0.17$ eV.

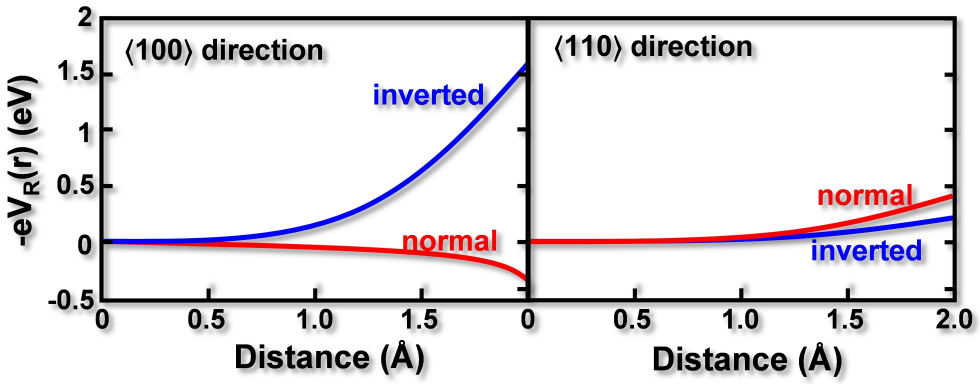

Figure 13. Electrostatic energy $-eV_R(\mathbf{r})$ associated with the internal field $E_R(\mathbf{r})$ along the two ⟨100⟩ and ⟨110⟩ directions in $KMgF_3$ (normal cubic perovskite, red curves) and $LiBaF_3$ (inverted perovskite, blue curves).

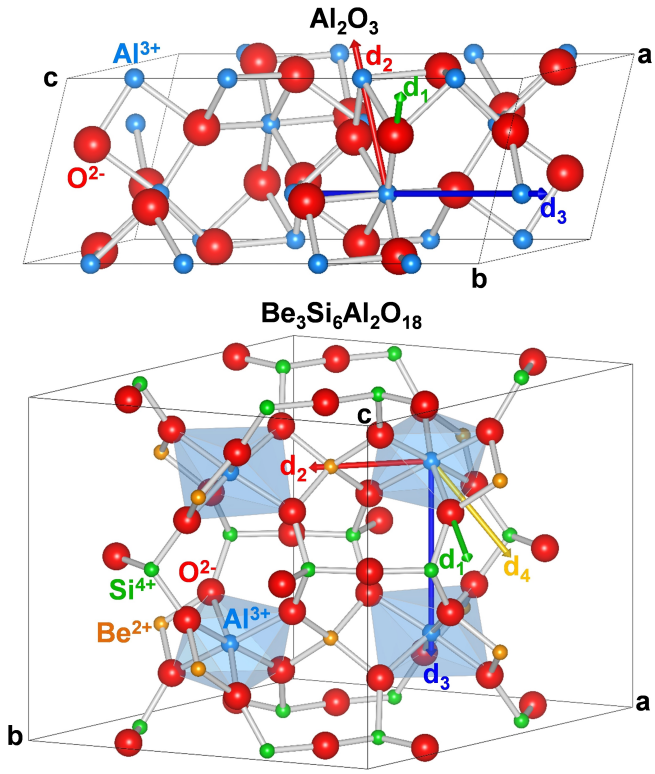

Figure 15. Structures of the host lattices of ruby ($Al_2O_3:Cr^{3+}$) and emerald ($Be_3Si_6Al_2O_{18}:Cr^{3+}$). The space groups of ruby, emerald are R3c, P6/mcc respectively. d_i (i = 1–4) arrows point out different directions in the CrO_6^{9-} complexes.

Seeking to better visualize the influence of $V_R(\mathbf{r})$ upon the electronic transitions, the excitation spectra of $KMgF_3:Mn^{2+}$ and $LiBaF_3:Mn^{2+}$ in the 1.75–3.25 eV range are displayed on Figure 14. In that figure, the three lowest transitions for a MnF_6^{4-} unit are observed.[11,52,54] The first two, $^6A_{1g}\rightarrow{}^4T_{1g}$ and $^6A_{1g}\rightarrow{}^4T_{2g}$, are 10Dq dependent, while the third one, $^6A_{1g}\rightarrow{}^4A_{1g}$, ^4E_g is 10Dq independent, thus much sharper.[11] As for MnF_6^{4-}, the value of 10Dq is roughly given by the energy difference of first and third transitions. Figure 14 clearly shows the increase of 10Dq when we move from $KMgF_3:Mn^{2+}$ to $LiBaF_3:Mn^{2+}$. Interestingly, the position of the sharp $^6A_{1g}\rightarrow{}^4A_{1g}$, ^4E_g transition is practically unmodified along the series of normal perovskites containing Mn^{2+} such as $KMgF_3:Mn^{2+}$, $RbMnF_3$ or $CsCaF_3:Mn^{2+}$ being found at 3.12 eV.[52,116,118] By contrast, that transition appears at 2.99 eV for $LiBaF_3:Mn^{2+}$,[54] thus implying a negative shift of 4%. This fact underlines that $V_R(\mathbf{r})$ also influences the covalency in the MnF_6^{4-} unit, thus the values of Racah parameters.[119]

4.2. Origin of the Different Color of Ruby, Emerald and Cr_2O_3

Another relevant example revealing the importance of the electrostatic potential $V_R(\mathbf{r})$ on the optical spectra of transition metal compounds concerns the origin of the distinct color of ruby ($Al_2O_3:Cr^{3+}$) and emerald ($Be_3Si_6Al_2O_{18}:Cr^{3+}$). In both gemstones, the characteristic color appears when doping with Cr^{3+} impurities, which enter the lattices replacing Al^{3+} ions, forming CrO_6^{9-} complexes.[44] The structural arrangements of the pure host lattices[44,46,47,120] are represented in Figure 15. As we will see later, the effect of $V_R(\mathbf{r})$ on the active electrons localized in a CrO_6^{9-} unit elucidates the underlying reasons for the different color exhibited by ruby and emerald.

In the case of green emerald, the six oxygen ions are *equidistant* from Cr^{3+} cation, with R = 1.97 Å as derived from EXAFS measurements.[47] The complex exhibits a slightly trigonally distorted geometry, with D_3 local symmetry. On the other hand, the CrO_6^{9-} complex in the red ruby displays a lower C_3 local symmetry, where three oxygen ions are placed at a short distance R_s=1.92 Å, the other three at a longer distance R_l=2.01 Å, according to EXAFS data.[46] The calculated metal-ligand distances for both ruby and emerald (Table 7) coincide with those determined by EXAFS. Such results imply that the *average* metal-ligand distance for ruby is 1.97 Å, thus equal to that reported for the emerald. This situation is quite reasonable as the average Al–O distance for Al_2O_3, $Be_3Si_6Al_2O_{18}$ is the same within 0.01 Å.

Regarding the optical absorption spectra in the Visible region (Figure 16), the distinctive colors of ruby (red) and emerald (green) are due to the shift of regions with minimum absorption on going from the first to the second gemstone. As shown on Figure 16, when the photon energy lies in the 12500 cm^{-1}–26000 cm^{-1} (or equivalently 1.55 eV–3.22 eV) range, there are two broad absorption bands of the CrO_6^{9-} complexes, assigned by the LFT to the spin allowed electronic transitions $^4A_{2g}\rightarrow{}^4T_{2g}$ and $^4A_{2g}\rightarrow{}^4T_{1g}$, peaked at 2.24 eV and 3.09 eV for ruby and 2.00 eV and 2.99 eV, for emerald (Figure 16). In both systems, the second band falls almost completely in the blue region, so that the main contribution to

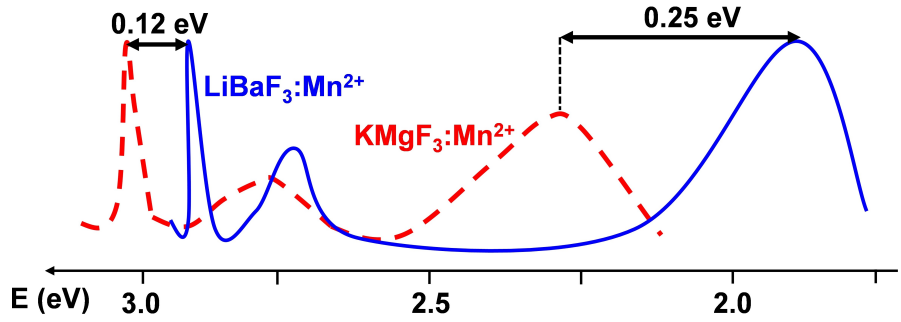

Figure 14. Excitation spectra of $KMgF_3:Mn^{2+}$ and $LiBaF_3:Mn^{2+}$ in the 1.75–3.25 eV range.

Table 7. Experimental and calculated Cr^{3+}–O^{2-} distances in CrO_6^{9-} complexes embedded in Al_2O_3 and $Be_3Si_6Al_2O_{18}$ pure lattices.

	R_s	R_l	Ref.
Al_2O_3 (exp)	1.857	1.969	[44,46]
$Al_2O_3:Cr^{3+}$ (exp)	1.92	2.01	[46]
$Al_2O_3:Cr^{3+}$ (calculated)	1.95	2.00	[46]
$Al_2O_3:Cr^{3+}$ (calculated)	1.942	1.997	[48]
$Be_3Si_6Al_2O_{18}$ (exp)	1.903	1.903	[47,120]
$Be_3Si_6Al_2O_{18}:Cr^{3+}$ (exp)	1.97	1.97	[47]
$Be_3Si_6Al_2O_{18}:Cr^{3+}$ (calculated)	1.968	1.968	[48]

Table 8. Values of the cubic field splitting 10Dq (in eV) in CrO_6^{9-} complexes in ruby and emerald calculated at experimental geometries.[48] Calculations were performed for isolated CrO_6^{9-} units and also including the electrostatic potential $V_R(\mathbf{r})$ originated by the ions located outside the complex. Experimental values are also included.

	isolated	$+V_R(r)$	exp. [46,47]
$Al_2O_3:Cr^{3+}$	2.00	2.25	2.24
$Be_3Si_6Al_2O_{18}:Cr^{3+}$	2.00	1.95	2.00

the difference in color between ruby, emerald comes from the displacement of the first band, $^4A_{2g}\rightarrow{}^4T_{2g}$. According to the LFT, the value of this transition is equal to 10Dq[11]. In 1957, Orgel[121] proposed that the difference in absorption bands must be related to the different average Cr–O distance, R, between ruby and emerald. Assuming Eq. (16) with an exponent n = 4.5, he suggested that R(emerald)-R(ruby) should be around 0.05 Å, indicating a larger compression when the complex is embedded in the corundum structure. However, later EXAFS measurements[46,47] challenged this assumption, since both ruby and emerald exhibited the *same average* Cr^{3+}–O^{2-} distance (Table 7). This result is consistent with the fact that in both systems Cr^{3+} replaces Al^{3+} and the average Al^{3+}–O^{2-} distance is practically the same (Table 7). An alternative explanation suggests that the unpaired electrons within the CrO_6^{9-} complex are not fully localized, with some electronic density extending beyond the first coordination sphere.[122] According to this view, the different value of 10Dq is attributed to a different electron charge flow beyond the first coordination sphere. Nevertheless, ENDOR measurements[51,53,88,89] and ab initio simulations[87,123] on ionic lattices, do not support a significant delocalization of electronic density over the second and further coordination spheres.

On the other hand, as we have demonstrated throughout this review, the internal electric field, $\mathbf{E}_R$, generated by the rest of lattice ions significantly affects the electrons within the MX_N complex. Therefore, it is crucial to consider the effects of this electric field, especially when dealing with non-cubic (section 3) or non-isomorphous lattices (section 4.1).

Table 8 presents the values of 10Dq parameter, including both the contribution from the isolated complex and the additional effect of the electrostatic potential $V_R(\mathbf{r})$. If the effect of the electrostatic potential is neglected, the difference between $(10Dq)_{int}$ values (Eq. 17) for ruby and emerald at the experimental distances is null, highlighting that in both gemstones the average metal-ligand distance is the same. However, when the electrostatic potential is considered, the associated contribution to 10Dq, denoted as $(10Dq)_{ext}$ (Eq. 17), amounts to 0.25 eV for ruby and −0.05 eV for emerald.[48] Consequently, the difference in the calculated value of 10Dq between the two gemstones increases to 0.30 eV. Notably, calculated and experimental values of 10Dq are remarkably similar, with differences smaller than 2%.

Figure 17 shows the electrostatic potential of ruby and emerald along the directions indicated in Figure 15. In 2012,

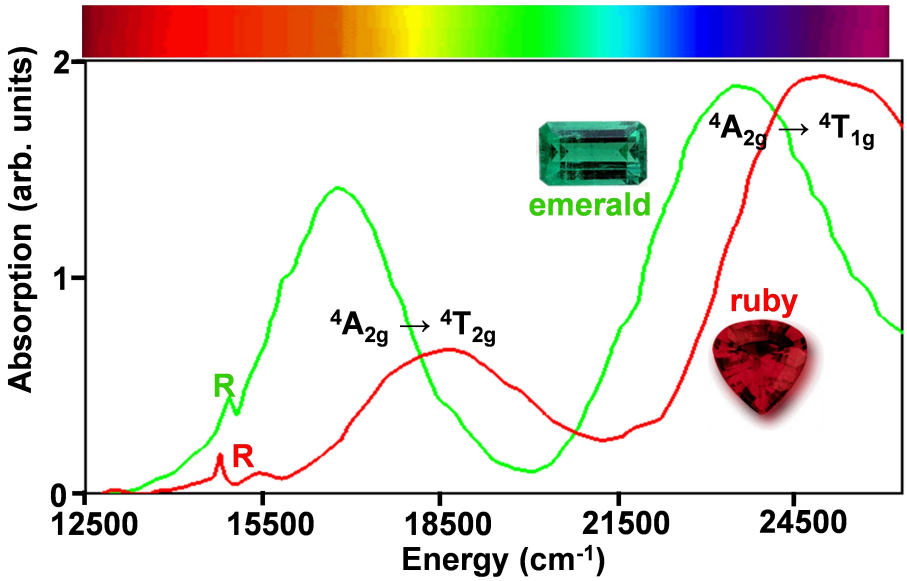

Figure 16. Optical absorption spectra of ruby and emerald in the Visible region,[44,45] indicating the electronic transitions corresponding to the two broad bands. The weak R line observed in the low energy region corresponds to the $^4A_{2g}\rightarrow{}^2E_g$ transition.

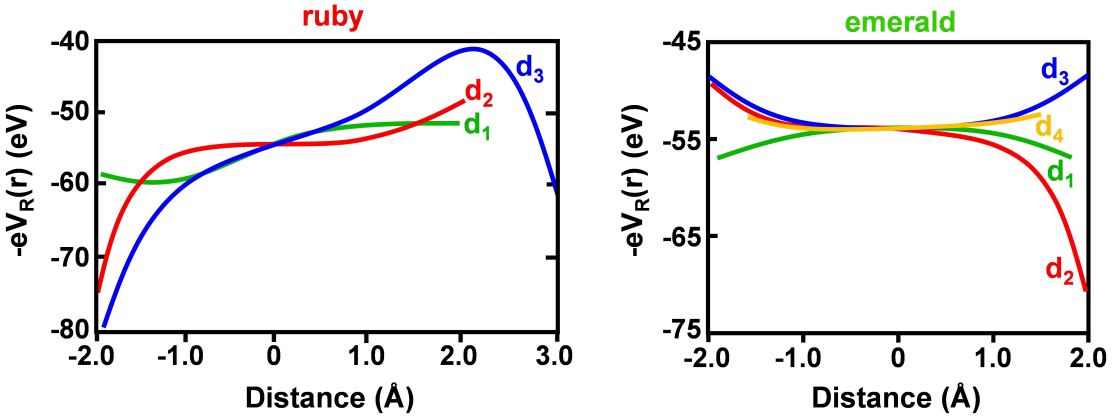

Figure 17. Electrostatic energy $-eV_R(\mathbf{r})$ of ruby and emerald along the d_i ($i=1$–4) directions of the respective CrO_6^{9-} complexes indicated in Figure 15.

Aramburu et al. developed a model for an octahedral system that provides insights into the differences observed between the two gemstones.[48] Using this model, they concluded that the variation in 10Dq arises from the *distinct nature of* $V_R(r)$ along different directions.

As it is shown on Figure 17, a closer examination reveals that in the case of ruby, the electrostatic potential $V_R(\mathbf{r})$ along the metal-ligand direction, d_1 (Figure 15), exhibits greater symmetry and softness compared to d_2, d_3 directions. Consequently, the t_{2g} orbital, which predominantly lies along d_2 and d_3 directions, experiences a greater decrease in energy compared to e_g orbital, which extends along d_1 direction. This qualitative analysis underscores how the electrostatic potential induces larger energy decrease in t_{2g} orbitals, thereby favoring the increase of 10Dq.

On the other hand, the variation of the electrostatic potential in emerald is generally less pronounced compared to that of ruby such as it can be seen on Figure 17. Regarding d_2, d_3 and d_4 directions (Figure 15), the effect of $V_R(\mathbf{r})$ is inhomogeneous. The electrostatic potential raises the energy along d_3 and d_4 directions, whereas it tends to decrease it along d_2 direction. However, the resulting variation in 10Dq is minimal in the case of emerald, suggesting a compensation of effects among the different directions. In the work by Aramburu et al, it is demonstrated that the small change in 10Dq induced by $V_R(\mathbf{r})$ arises from the practical cancellation of contributions originating from three Be^{2+} ions placed at 2.66 Å, six Si^{4+} ions at 3.31 Å.[48,49] These results further emphasize the relevance of internal electric fields[16,50] in understanding optical and many other properties of transition-metal compounds in insulating materials.

The spectra of Figure 16 also show the presence of the sharp R line that corresponds to the spin forbidden transition $^4A_{2g} \rightarrow {}^2E_g$.[2,44,45] Interestingly, this transition, independent of 10Dq,[11] is little sensitive to the nature of the host lattice as it appears practically at the same place for ruby (1.79 eV), emerald (1.82 eV). By contrast, the $^6A_{1g} \rightarrow {}^4A_{1g}$, ^4E_g transition for a MnF_6^{4-} unit, which is also 10Dq independent, is more sensitive to the change of crystal lattice with different structure[52,54] such as it is shown on Figure 14. This matter is discussed on Ref. [119].

To conclude this section, we address a noteworthy example concerning the effect of the internal electric field related to the progressive color shift from red to green in $Al_2O_3 \cdot xCr_2O_3$ when increasing the concentration of Cr^{3+} ions.[124,125] The crystal structure and the insulating character is kept along the series. It is worth noting that the metal-ligand distance, R, experiences an increase of only 0.75% in the transition from $Al_2O_3:Cr^{3+}$ (R=1.965 Å) to Cr_2O_3 (R=1.980 Å). Nonetheless, this small change of metal-ligand distance does not account for the observed variation in 10Dq parameter on passing from ruby (10Dq=2.24 eV) to pure Cr_2O_3 (10Dq=2.06 eV),[125] responsible for the color shift. Indeed, a R increase of 0.015 Å would lead to a decrease of the intrinsic contribution, $(10Dq)_{int}$, equal only to 0.07 eV. This quantity is thus less than one half the experimental value $\Delta(10Dq)$=0.18 eV.

Similar color shifts manifest in other insulating crystals, such as $MgAl_2O_4 \cdot xMgCr_2O_4$[126] or $YAl_2O_4 \cdot xYCr_2O_4$.[126] García-Lastra *et al.* demonstrated that, for $x<0.2$, the primary driving force behind the color shift is rooted in the reduction of the internal electric field experienced by the CrO_6^{9-} complex when the Al^{3+} ions are progressively replaced by Cr^{3+} ions[128] thus increasing the x value. As discussed below, this effect is a consequence of Pauling's electroneutrality principle,[129] which postulates that the total charge of the transition-metal cation within the complex is *nearly* zero.

If Cr^{3+} impurities in $Al_2O_3:Cr^{3+}$ are highly diluted, the first neighbors of a CrO_6^{9-} complex are Al^{3+} ions, whose actual charge is close to the nominal charge, +3e. However, as the concentration of Cr^{3+} ions increases, some of these ions progressively occupy lattice positions held by Al^{3+} ions, located near another CrO_6^{9-} complex. The core of the issue lies in the fact that the actual charge of Cr^{3+} ions within this lattice significantly deviates from that of Al^{3+}. This deviation arises from the open-shell nature of Cr^{3+} ion, so it can accept additional electron charge from O^{2-} ligands. This key fact is the basis of Pauling's electroneutrality principle.[129] In practice, the calculated value for the Al^{3+} charge in Al_2O_3 is $q_{Al}=2.6e$, while for Cr^{3+} in Cr_2O_3 is $q_{Cr}=1.3e$, half that of the Al^{3+}.[128] Thus, the progressive substitution of *nominal* Al^{3+} by Cr^{3+} ions in $Al_2O_3 \cdot xCr_2O_3$ implies a significant reduction of the *actual* charge

associated with the nominal trivalent ion, consequently a lessening of both the electrostatic potential, $V_R(\mathbf{r})$, and the extrinsic contribution $(10Dq)_{ext}$. Therefore, the diminution of $(10Dq)_{ext}$ along the $Al^{3+} \rightarrow Cr^{3+}$ substitution is the main responsible for the color shift observed when comparing ruby and pure Cr_2O_3 such as it has been proved.[128]

4.3. Big Effect of the Internal Electric Field for Explaining the Color of the Egyptian Blue Pigment

In the world of prehistoric art, the absence of blue hues is a widely recognized fact.[56,58,130–132] Hence, these cultures did not have the appropriate pigments to produce this color. In fact, while the rest of the palette could be obtained through iron and manganese oxides and coal, prehistoric men were not able to get stable minerals displaying a deep blue color. The only known blue pigment in ancient times was the rare gemstone lapis lazuli, which was mined in far Afghanistan. However, around 3600 BC, the Egyptian culture was able to synthesize the first pigment, the so-called Egyptian Blue, which was later transmitted throughout the Mediterranean cultures.[56–58,130–132] This section is focused on explaining the microscopic origin of the distinctive blue color exhibited by this pigment, as can be observed in paintings in Amarna, Luxor, or Pompeii archeological sites, with the crown of the famous bust of Queen Nefertiti, exhibited in the Neues Museum of Berlin, being the best-known example where pure Egyptian Blue was used.

The synthesis process of Egyptian Blue involves a combination of cuprorivaite ($CaCuSi_4O_{10}$), unreacted quartz and varying amounts of glass.[56,130,131] Cuprorivaite, a layered compound displaying tetragonal P4/ncc structure[133] (Figure 18, left), serves as the primary component of the pigment. The square-planar CuO_4^{6-} complex contained in this material, with Cu–O distance R = 1.928 Å, is the chromophore responsible for the blue color. Interestingly, this hue is not observed in other lattices such as $CaCuO_2$ despite containing the same CuO_4^{6-} chromophore (Figure 18, right) with practically the same metal-ligand distance, R = 1.929 Å,[134] consistent with the fact that the Cu^{2+}–O^{2-} bond lengths in CuO_4^{6-} complexes are short and so they are very strong and similar in different lattices. This observation is in the same vein of what occurs when comparing ruby and emerald (section 4.2).

As can be inferred from the analysis presented in the previous sections, the role played by the electrostatic potential of the rest of lattice ions $V_R(\mathbf{r})$, strongly dependent on the crystal structure, is instrumental in understanding this behavior.[58,132] As demonstrated below, the large difference displayed by the shape of $V_R(\mathbf{r})$ in axial, equatorial directions of the CuO_4^{6-} unit emerges as the underlying cause of the exotic blue color of this compound.

Materials containing square-planar CuO_4^{6-} units exhibit three broad d–d transition bands that span a significant region of the optical spectrum (Figure 19).[135–137] Table 9 shows the experimental d–d transition energies for $CaCuSi_4O_{10}$ and $CaCuO_2$. A comparison between these compounds reveals that the Egyptian blue exhibits a peak corresponding to the highest $3z^2\text{-}r^2 \rightarrow x^2\text{-}y^2$ transition at 2.297 eV,[135,136] shifted by 0.353 eV compared to the corresponding transition peak in $CaCuO_2$.[137] Considering that the blue region is around 2.7 eV, $CaCuSi_4O_{10}$

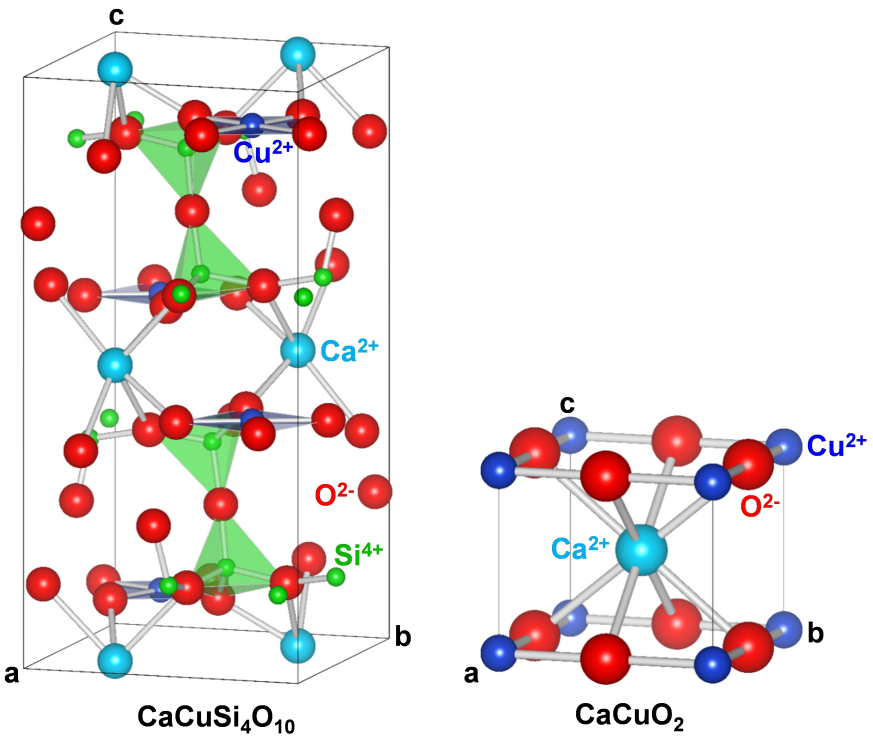

Figure 18. Structures of cuprorivaite ($CaCuSi_4O_{10}$), a layered compound displaying tetragonal P4/ncc space group and $CaCuO_2$. Both materials contain square-planar CuO_4^{6-} complexes.

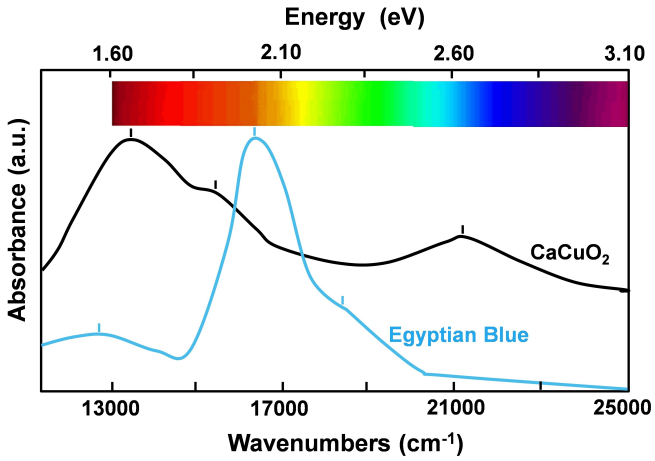

Figure 19. Absorption spectra in the Visible range of Egyptian Blue ($CaCuSi_4O_{10}$) and $CaCuO_2$. Marks underline the position of three d–d transitions in both compounds.

does not absorb the blue light, giving rise to its characteristic blue color. A similar behavior is observed in the Han Blue pigment $BaCuSi_4O_{10}$, developed during the Han dynasty (208 B.C.–220 A.D.) in China,[56,58] where the transition peak is found at 2.331 eV.[138]

Considering that the Cu–O distances in both $CaCuSi_4O_{10}$ and $CaCuO_2$ compounds are practically identical, differing by only 0.05%, it becomes challenging to explain the significant reduction of 0.353 eV in the energy of the highest d–d transition by means of LFT. According to LFT, such a reduction would need a smaller Cu–O distance in the $CaCuO_2$, which contradicts experimental R values in both compounds that are essentially identical. Hence, the optical properties of Egyptian blue pigments cannot be understood by considering only the changes within the CuO_6^{4-} chromophore.

As shown in Table 9, the expected value for the $3z^2\text{-}r^2 \rightarrow x^2\text{-}y^2$ transition in the *isolated* CuO_6^{4-} complex is approximately 3.311 eV, significantly higher than those measured for $CaCuSi_4O_{10}$ or $CaCuO_2$. However, calculations incorporating the electrostatic potential of the rest of lattice ions demonstrate a considerable energy reduction of 0.561 eV and 0.880 eV for $CaCuO_2$ and $CaCuSi_4O_{10}$, respectively. This fact reveals a strong correlation between d–d transitions and the form of the $V_R(\mathbf{r})$ potential. The observed energy shifts can be qualitatively understood by examining the shape of the electrostatic potential in the two lattices, represented in Figure 20. The electrostatic potential $V_R(\mathbf{r})$ is depicted along both the Cu–O and the axial directions of the CuO_4^{6-} unit, since the orbitals involved in the highest d–d transition, $3z^2\text{-}r^2$ and $x^2\text{-}y^2$, primarily extend along such directions. The electrostatic potential in both $CaCuSi_4O_{10}$ and $CaCuO_2$, displayed in Figure 20, has the tendency to increase the energy of $3z^2\text{-}r^2$ and decrease that of $x^2\text{-}y^2$, thereby qualitatively explaining the energy reduction observed when including $V_R(\mathbf{r})$ in the calculations. However, there are notable quantitative differences between the two systems. The effect of $V_R(\mathbf{r})$ is more pronounced in $CaCuSi_4O_{10}$, reflecting the greater difference between the axial and equatorial directions in this compound, which exhibits higher anisotropy. As a result of this anisotropy, $CaCuSi_4O_{10}$ exhibits its distinctive blue color.[58]

Table 9. Calculated energies (in eV) of d–d optical transitions i) for an isolated CuO_4^{6-} complex at R = 1.928 Å and ii) adding the effects of the electrostatic potential $V_R(\mathbf{r})$ corresponding to $CaCuSi_4O_{10}$ and $CaCuO_2$. The experimental transition energies for $CaCuSi_4O_{10}$[135,136] and $CaCuO_2$[137] are also given for comparison.

Transition	CuO_4^{6-} isolated	$CaCuSi_4O_{10}$ calculated	$CaCuSi_4O_{10}$ experim.	$CaCuO_2$ calculated	$CaCuO_2$ experim.
$xy \rightarrow x^2\text{-}y^2$	1.749	1.489	1.580	1.538	1.639
$xz, yz \rightarrow x^2\text{-}y^2$	2.331	1.980	2.000	1.935	1.949
$3z^2\text{-}r^2 \rightarrow x^2\text{-}y^2$	3.311	2.431	2.297	2.750	2.650

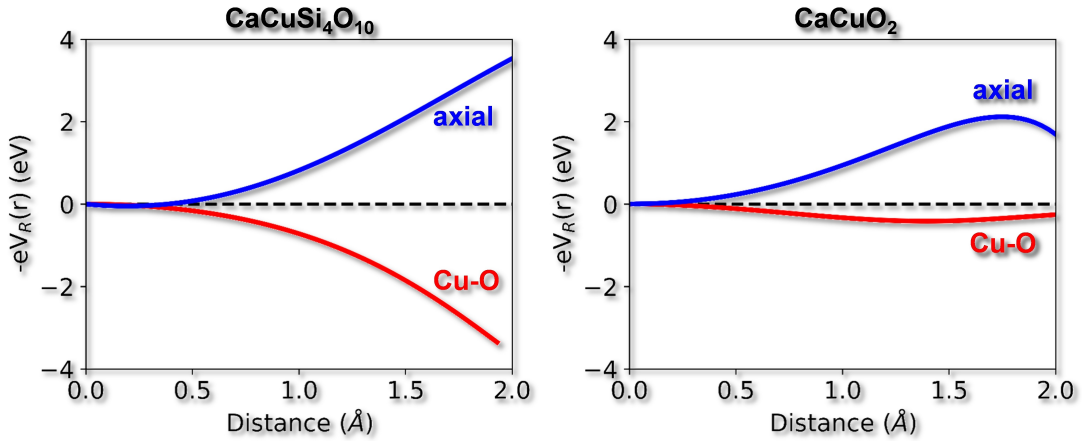

Figure 20. Electrostatic energies $-eV_R(\mathbf{r})$ of $CaCuSi_4O_{10}$ and $CaCuO_2$ along Cu–O in-plane and axial directions.

Significant research on Egypt, Chinese blue pigments is currently being carried out.[139–143]

5. Summary and Outlook

Although in insulating TM compounds active electrons are essentially localized in the MX_N complex, their optical properties cannot, in general, be explained considering only that *isolated* unit such as it has been emphasized in this review work. Indeed, as the rest of the lattice is composed of ions they give rise to an internal field, $E_R(\mathbf{r})$, that is sensitive to the crystal structure and modifies the energy levels of the MX_N complex. For this reason, the effects of $E_R(\mathbf{r})$, usually not considered in books,[2,9,10,44] are specially well seen when comparing the optical response of the same complex placed in two lattices with different crystal structure. As it has been shown in section 4.2, $E_R(\mathbf{r})$, plays a central role for understanding the actual origin of the different color due to a Cr^{3+} impurity in oxides like Al_2O_3 or $Be_3Si_6Al_2O_{18}$, as well as in $BeAl_2O_4$,[144] $MgAl_2O_4$[145] or MgO.[49]

The internal electric field also plays a relevant role for d^9 ions placed in tetragonal lattices like K_2MgF_4 or K_2ZnF_4, where the octahedron surrounding the divalent cation is nearly perfect. In such cases, the shape of $V_R(\mathbf{r})$ has a great influence on the nature of the ground state. We have seen in section 3.1 that for Cu^{2+} doped K_2ZnF_4 $V_R(\mathbf{r})$ helps to locate the hole in an $a_{1g}(3z^2\text{-}r^2)$ orbital, a fact which in turn tends to reduce the axial Cu^{2+}–F^- distance producing a kind of compressed geometry not due to the Jahn-Teller effect. On the contrary, in the case of La_2CuO_4, $V_R(\mathbf{r})$ tends to stabilize $b_{1g}(3z^2\text{-}r^2)$ as the hole level in the ground state, thus favoring an elongated geometry.[82]

It is worth noting now that $V_R(\mathbf{r})$ plays a minor role concerning the nature of ground state in cases like K_2ZnF_4:Ni^{2+} or K_2NiF_4 involving NiF_6^{4-} units. Indeed, its wavefunction for S = 1, M = 1 is always $|a_{1g}\uparrow, b_{1g}\uparrow|$ independently of the electron level with lowest energy and consequently the local geometry around Ni^{2+} can be nearly octahedral.

Another relevant conclusion of the present work concerns the origin of local distortions in insulating compounds containing d^9 or d^4 ions. Indeed, it has been shown that, in most cases, they do not arise from a Jahn-Teller effect despite it is widely believed.[12,28,29,94,146,147] In particular, in systems containing initially tetragonal CuX_6^{4-} units (X=halide) with a compressed geometry, the system can become unstable until reaching a final orthorhombic geometry.

Interestingly, this change of equilibrium geometry also involves a parallel change of the electronic density which, according to Eq. (15), requires the existence of excited states that can be mixed with the ground state through the operator $V_\Gamma(\mathbf{r})$, reflecting the electron-vibration interaction. It should be emphasized now that as that operator is purely orbital, the excited states must have the same spin as the ground state. This condition is well fulfilled for tetragonal CuX_6^{4-} units (X=halide) where a $^2A_{1g}$ state can be mixed with $^2B_{1g}$ if $V_\Gamma(\mathbf{r})$ belongs to B_{1g}. However, in a MnX_6^{4-} unit with a S=5/2 ground state, none of the rest of 246 states emerging from the d^5 configuration has a S=5/2.[11] This *spin barrier* is thus against the existence of an orthorhombic distortion in K_2MnF_4 which is however well observed for K_2CuF_4 or Cs_2AgF_4.[148] Along this line, it has recently been proved[149] that the local orthorhombic geometry in those compounds is the source of their surprising ferromagnetic behavior in contrast to the antiferromagnetism exhibited by K_2MnF_4, K_2NiF_4 or $KNiF_3$.[150]

In the present work the instability driven by vibronic interactions has been focused on the orthorhombic distortion taking place in systems like K_2CuF_4 or $(C_2H_5NH_3)_2CdCl_4$:Cu^{2+}. Nevertheless, there are cases where the structural instability can lead to a huge displacement of ions an even a change of coordination number.[8] That situation is found for $SrCl_2$:Cu^{2+} where copper ion moves off-center 1.3 Å along a $<100>$ type direction from the Sr^{2+} site, thus changing the coordination number from 8 to 4.[151,152]

As the right interpretation of experimental data is crucial in science, one should avoid the use of speculations or assumptions not fully supported. Accordingly, explanations based on parametrized models with fitting parameters or the idea that any distortion associated with d^9 or d^4 complexes *necessarily* comes from the Jahn-Teller effect are, in general, meaningless. Indeed, for having a Jahn-Teller effect, the initial geometry of a MX_6^{4-} unit (M=Cu^{2+}, Ag^{2+}) should be cubic or even trigonal[14,67,83,153] but not tetragonal or monoclinic. When this symmetry rule is not fulfilled, first-principles calculations can be of great help for revealing the actual origin of the local structure, such as it has been shown in this work.

In particular, they can be very useful for understanding the effects of high pressures on optical properties of insulating TM compounds. Indeed, they provide a key information on the variation of metal-ligand distances with pressure that it is not always easy to obtain from X-ray data.

Further work along this line is now underway.

Acknowledgements

The authors acknowledge financial support from Grant No. PGC2018-096955-B-41 funded by MCIN/AEI/10.13039/501100011033. I. S.-M. (grant BDNS:589170) acknowledges financial support from Universidad de Cantabria and Gobierno de Cantabria.

Conflict of Interests

The authors declare no conflict of interest.

Data Availability Statement

Data sharing is not applicable to this article as no new data were created or analyzed in this study.

Keywords: internal electric field · optical properties · transition metal ions · vibronic instabilities

[1] P. F. Moulton, *J. Opt. Soc. Am. B* **1986**, *3*, 125–133.
[2] R. C. Powell, *Physics of solid-state laser materials*, Springer, New York **1998** pp. 1–9, 215.
[3] M. E. Doroshenko, V. V. Osiko, H. Jelínková, M. Jelínek, J. Šulc, D. Vyhlídal, N. O. Kovalenko, I. S. Terzin, *Opt. Mater. Express* **2018**, *8*, 1708–1722.
[4] R. J. Singh, *J. Mod. Phys.* **2013**, *4*, 191–199.
[5] X. Li, X. Zhong, Y. Hu, B. Li, Y. Sheng, Y. Zhang, C. Weng, M. Feng, H. Han, J. Wang, *J. Phys. Chem. Lett.* **2017**, *8*, 1804–1809.
[6] A. Jaffe, Y. Lin, W. L. Mao, H. I. Karunadasa, *J. Am. Chem. Soc.* **2015**, *137*, 1673–1678.
[7] S. Gupta, T. Pandey, A. K. Singh, *Inorg. Chem.* **2016**, *55*, 6817–6824.
[8] M. Moreno, M. T. Barriuso, J. A. Aramburu, P. García-Fernández, J. M. García-Lastra, *J. Phys. Condens. Matter* **2006**, *18*, R315–R360.
[9] J. S. Griffith, *The theory of transition-metal ions*, Cambridge, Cambridge **1961** pp. 182–319.
[10] A. P. Lever, *Inorganic electronic spectroscopy*, Elsevier, Amsterdam **1984** pp. 98–160.
[11] S. Sugano, Y. Tanabe, H. Kamimura, *Multiplets of transition metal ions in crystals*, Academic Press, New York **1970** pp. 126–153, 263–270.
[12] D. Reinen, *Inorg. Chem.* **2012**, *51*, 4458–4472.
[13] P. García-Fernández, A. Trueba, M. T. Barriuso, J. A. Aramburu, M. Moreno, *Prog. Theor. Chem. Phys.* **2011**, *23*, 105–142.
[14] F. S. Ham in *Electron Paramagnetic Resonance*, (Ed.: S. Geschwind), Plenum: New York **1972** pp. 1–119.
[15] J. M. García-Lastra, J. A. Aramburu, M. T. Barriuso, M. Moreno, *Phys. Rev. Lett.* **2004**, *93*, 226402.
[16] J. M. García-Lastra, M. T. Barriuso, J. A. Aramburu, M. Moreno, *Phys. Rev. B* **2005**, *72*, 113104.
[17] I. B. Bersuker, N. N. Gorinchoi, V. Z. Polinger, *Theor. Chim. Acta* **1984**, *66*, 161–172.
[18] J. A. Aramburu, P. García-Fernández, N. R. Mathiesen, J. M. García-Lastra, M. Moreno, *J. Phys. Chem. C* **2018**, *122*, 5071–5082.
[19] E. M. C. Minner, *Ph.D. Thesis*, University of Geneva (Geneva), **1993**.
[20] L. Dubicki, M. J. Riley, E. R. Krausz, *J. Chem. Phys.* **1994**, *101*, 1930–1939.
[21] M. J. Riley, L. Dubicki, G. Moran, E. R. Krausz, *Chem. Phys.* **1990**, *14*, 363–373.
[22] J. A. Aramburu, J. M. García-Lastra, P. García-Fernández, M. T. Barriuso, M. Moreno, *Inorg. Chem.* **2013**, *52*, 6923–6933.
[23] I. Yamada, *J. Phys. Soc. Jpn.* **1972**, *33*, 979–988.
[24] M. J. Riley, L. Dubicki, G. Moran, E. R. Krausz, I. Yamada, *Inorg. Chem.* **1990**, *29*, 1614–1626.
[25] P. García-Fernández, M. T. Barriuso, J. M. García-Lastra, M. Moreno, J. A. Aramburu, *J. Phys. Chem. Lett.* **2013**, *4*, 2385–2390.
[26] P. Fischer, W. Haelg, D. Schwarzenbach, H. Gamsjaeger, *J. Phys. Chem. Solids* **1974**, *35*, 1683–1689.
[27] D. Oelkrug, *Struct. Bonding (Berlin)* **1971**, *9*, 1–26.
[28] A. F. Wells, *Structural Inorganic Chemistry*, Oxford **1975**, pp. 204, 277–278.
[29] D. Reinen, S. Krause, *Inorg. Chem.* **1981**, *20*, 2750–2759.
[30] T. Chatterji, Th. C. Hansen, *J. Phys. Condens. Matter* **2011**, *23*, 276007–276015.
[31] J. A. Aramburu, M. Moreno, *Inorg. Chem.* **2019**, *58*, 4609–4618.
[32] K. H. Jack, R. Maitland, *Proc. Chem. Soc. London* **1957**, 232.
[33] P. E. Lim, J. W. Stout, *J. Chem. Phys.* **1975**, *63*, 4886–4902.
[34] J. A. Aramburu, M. Moreno, *Phys. Chem. Chem. Phys.* **2019**, *21*, 11714–11723.
[35] G. Wingefeld, R. Hoppe, *Z. Anorg. Allg. Chem.* **1984**, *516*, 223.
[36] K. Finnie, L. Dubicki, E. R. Krausz, M. J. Riley, *Inorg. Chem.* **1990**, *29*, 3908–3910.
[37] M. Atanasov, M. A. Hitchman, R. Hoppe, S. Keith, S. Murray, B. Moubaraki, D. Reinen, H. Stratemeier, *Inorg. Chem.* **1993**, *32*, 3397–3401.
[38] Z. Mazej, I. Arcon, P. Benkic, A. Kodre, A. Tressaud, *Chem. Eur. J.* **2004**, *10*, 5052–5058.
[39] J. A. Aramburu, M. Moreno, *Inorg. Chem.* **2020**, *59*, 539–547.
[40] J. P. Steadman, R. D. Willett, *Inorg. Chim. Acta* **1970**, *4*, 367–371.
[41] R. Valiente, F. Rodriguez, J. A. Aramburu, M. Moreno, M. T. Barriuso, C. Sousa, C. De Graaf, *Int. J. Quantum Chem.* **2002**, *86*, 239–244.
[42] A. R. Lim, L. K. Kwac, *Sci. Rep.* **2022**, *12*, 8769.
[43] D. Carrasco-Busturia, I. Sánchez-Movellán, A. S. Tygesen, A. Bhowmik, J. M. García-Lastra, J. A. Aramburu, M. Moreno, *Chem. Eur. J.* **2023**, *29*, e202202933.
[44] R. G. Burns, *Mineralogical applications of crystal field theory*, Cambridge University Press, Cambridge, **1993** p.
[45] S. J. Duclos, Y. K. Vohra, A. L. Ruoff, *Phys. Rev. B* **1990**, *41*, 5372.
[46] E. Gaudry, A. Kiratisin, P. Sainctavit, C. Brouder, F. Mauri, A. Ramos, A. Rogalev, J. Goulon, *Phys. Rev. B* **2003**, *67*, 094108.
[47] E. Gaudry, D. Cabaret, C. Brouder, I. Letard, A. Rogalev, F. Wilhlem, N. Jaouen, P. Sainctavit, *Phys. Rev. B* **2007**, *76*, 094110.
[48] J. A. Aramburu, P. García-Fernández, J. M. García-Lastra, M. T. Barriuso, M. Moreno, *Phys. Rev. B* **2012**, *85*, 245118.
[49] J. A. Aramburu, P. García-Fernández, J. M. García-Lastra, M. T. Barriuso, M. Moreno, *J. Phys. Condens. Matter* **2013**, *25*, 175501.
[50] M. O. J. Y. Hunault, Y. Harada, J. Miyawaki, J. Wang, A. Meijerink, F. M. F. De Groot, M. M. Van Schooneveld, *J. Phys. Chem. A* **2018**, *122*, 4399–4413.
[51] R. K. Jeck, J. J. Krebs, *Phys. Rev. B* **1972**, *5*, 1677.
[52] F. Rodriguez, M. Moreno, A. Tressaud, J. P. Chaminade, *Cryst. Lattice Defects Amorphous Mater.* **1987**, *16*, 221–225.
[53] T. Yosida, *J. Phys. Soc. Jpn.* **1980**, *49*, 127.
[54] B. Henke, M. Secu, U. Rogulis, S. Schweizer, J. M. Spaeth, *Phys. Status Solidi C* **2005**, *2*, 380.
[55] A. Trueba, J. M. García-Lastra, M. T. Barriuso, J. A. Aramburu, M. Moreno, *Phys. Rev. B: Condens. Matter Mater. Phys.* **2008**, *78*, 075108.
[56] H. Berke, *Chem. Soc. Rev.* **2007**, *36*, 15–30.
[57] T. Rajaramanan, M. Keykhaei, F. Heidari Gourji, P. Ravirajan, M. Senthilnanthanan, Ø. Frette, D. Velauthapillai, *Mater. Adv.* **2023**, *4*, 4344.
[58] P. García-Fernandez, M. Moreno, J. A. Aramburu, *Inorg. Chem.* **2015**, *54*, 192–199.
[59] R. T. Poole, J. G. Jenkin, J. Liesegang, R. C. G. Leckey, *Phys. Rev. B* **1975**, *11*, 5179–5189.
[60] M. Kitamura, S. Muramatsu, *Phys. Rev.* **1990**, *41*, 1158–1172.
[61] J. A. Aramburu, M. Moreno, I. Cabria, M. T. Barriuso, C. Sousa, C. De Graaf, F. Illas, *Phys. Rev.* **2000**, *62*, 13356–13365.
[62] P. Greenough, A. G. Paulusz, *J. Chem. Phys.* **1979**, *70*, 1967.
[63] P. A. Tanner, *Chem. Phys. Lett.* **2004**, *388*, 488–493.
[64] H. Vercammen, D. Schoemaker, B. Briat, F. Ramaz, F. Callens, *Phys. Rev. B* **1999**, *59*, 11286.
[65] M. T. Barriuso, P. García-Fernández, J. A. Aramburu, M. Moreno, *Solid State Commun.* **2001**, 120.
[66] J. M. Garcia-Lastra, M. T. Barriuso, J. A. Aramburu, M. Moreno, *Chem. Phys.* **2005**, *317*, 103–110.
[67] A. Abragam, B. Bleaney, *Electron paramagnetic resonance of transition Ions*, Clarendon Press, Oxford **1970**, pp. 461.
[68] J. M. Jacobsen, B. M. Tissue, W. M. Yen, *J. Phys. Chem.* **1992**, *96*, 1547.
[69] R. E. Coffman, *J. Chem. Phys.* **1968**, *48*, 609–618.
[70] M. J. Riley, C. J. Noble, P. L. W. Tregenna-Piggott, *J. Chem. Phys.* **2009**, *130*, 104708.
[71] A. Boatner, R. W. Reynolds, M. M. Abraham, Y. Chen, *Phys. Rev. Lett.* **1973**, *31*, 7–10.
[72] P. García-Fernández, A. Trueba, M. T. Barriuso, J. A. Aramburu, M. Moreno, *Phys. Rev. Lett.* **2010**, *104*, 035901.
[73] U. Opik, M. H. M. Pryce, *Proc. R. Soc. London Ser. A* **1957**, *238*, 425–447.
[74] P. Garcia-Fernandez, I. B. Bersuker, J. A. Aramburu, M. T. Barriuso, M. Moreno, *Phys. Rev. B: Condens. Matter Mater. Phys.* **2005**, *71*, 184117.
[75] W. Low, J. T. Suss, *Phys. Lett.* **1963**, *7*, 310–312.
[76] J. A. Aramburu, P. García-Fernández, J. M. García-Lastra, M. Moreno, *ChemPhysChem* **2016**, *17*, 2146–2156.
[77] R. H. Borcherts, H. Kanzaki, H. Abe, *Phys. Rev. B* **1970**, *2*, 23–27.
[78] I. Sánchez-Movellán, J. A. Aramburu, M. Moreno, *Phys. Chem. Chem. Phys.* **2020**, *22*, 7875–7887.
[79] J. A. Aramburu, P. García-Fernández, J. M. García-Lastra, M. Moreno, *J. Phys. Chem. C* **2017**, *121*, 5215–5224.
[80] J. Dutta, S. Adhikari, N. N. Kovaleva, *J. Chem. Phys.* **2019**, *150*, 064703.
[81] J. Dutta, S. Ravi, S. Mukherjee, A. K. Ojha, S. Adhikari, *J. Phys. Chem. A* **2022**, *126*, 691–709.
[82] P. García-Fernández, M. Moreno, J. A. Aramburu, *J. Phys. Chem. C* **2014**, *118*, 7554–7561.
[83] E. Minner, D. Lovy, H. Bill, *J. Chem. Phys.* **1993**, *99*, 6378–6383.
[84] R. Hord, G. Cordier, K. Hoffmann, A. Buckow, G. Pascua, H. Luetkens, L. Alff, B. Albert, *Phys. Rev. B* **2010**, *82*, 180508.
[85] J. A. Aramburu, A. Bhowmik, J. M. García-Lastra, P. García-Fernández, M. Moreno, *J. Phys. Chem. C* **2019**, *123*, 3088–3101.
[86] I. B. Bersuker, *The Jahn-Teller Effect*, Cambridge University Press, Cambridge **2006**, pp. 110–112.
[87] J. M. García-Lastra, J. Y. Buzaré, M. T. Barriuso, J. A. Aramburu, M. Moreno, *Phys. Rev. B* **2007**, *75*, 155101.

[88] N. Laurance, E. C. McIrvine, J. Lambe, *J. Phys. Chem. Solids* **1962**, *23*, 515.
[89] D. Bravo, R. Bottcher, *J. Phys. Condens. Matter* **1992**, *4*, 7295.
[90] M. J. Colaneri, J. Vitali, *J. Phys. Chem. A* **2021**, *125*, 3268–3278.
[91] C. K. Jørgensen, *Modern Aspects of Ligand Field Theory*, North Holland, Amsterdam **1971**.
[92] E. N. Maslen, N. Spadaccini, T. Ito, F. Marumo, K. Tanaka, Y. Satow, *Acta Crystallogr. Sect. C* **1988**, *44*, 1707–1709.
[93] E. Herdtweck, D. Babel, *Z. Kristallogr.* **1980**, *153*, 189–199.
[94] D. Babel, A. Tressaud, in *Inorganic Solid Fluorides*, (Ed.: P. Hagenmuller), Academic Press, New York **1985**.
[95] M. Hidaka, K. Inoue, I. Yamada, P. J. Walker, *Physica B: Condensed Matter* **1983**, *121*, 343–350.
[96] G. Parr, W. Yang, in *Density-Functional Theory of Atoms, Molecules*, Oxford, New York **1989**, p. 141.
[97] A. Ceulemans, *The Theory of the Jahn-Teller Effect: When a Boson meets a Fermion*, Springer Nature: Cham, Switzerland **2022**, p. 4.
[98] N. O'Toole, V. Streltsov, *Acta Crystallogr. Sect. B* **2001**, *57*, 128–135.
[99] J. D. Swalen, B. Johnson, H. M. Gladney, *J. Chem. Phys.* **1970**, *52*, 4078–4086.
[100] I. Pabst, H. Fuess, J. W. Bats, *Cryst. Struct. Commun.* **1987**, *43*, 413–416.
[101] F. Barendregt, H. Schenk, *Physica* **1970**, *49*, 465–468.
[102] Y. Moritomo, Y. Tokura, *J. Chem. Phys.* **1994**, *101*, 1763–1766.
[103] R. Kentsch, M. Scholz, K. Oum, T. Lenzer, *J. Phys. Chem. C* **2023**, *127*, 22222–22233.
[104] M. Y. Choi, S. J. Lee, H. Ju, A. R. Lim, *RSC Adv.* **2022**, *12*, 20679.
[105] A. Trueba, P. García-Fernández, J. M. García-Lastra, J. A. Aramburu, M. T. Barriuso, M. Moreno, *J. Phys. Chem. A* **2011**, *115*, 1423–1432.
[106] S. R. Desjardins, K. W. Penfield, S. L. Cohen, R. L. Musselman, E. I. Solomon, *J. Am. Chem. Soc.* **1983**, *105*, 4590.
[107] M. A. Hitchman, P. J. Cassidy, *Inorg. Chem.* **1979**, *18*, 1745.
[108] R. G. McRonald, M. A. Hitchman, *Inorg. Chem.* **1986**, *25*, 3273.
[109] J. A. Aramburu, M. Moreno, A. Bencini, *Chem. Phys. Lett.* **1987**, *140*, 462–467.
[110] G. Chapuis, *Phys. Status Solidi A* **1977**, *43*, 203–208.
[111] C. Furlani, A. Sgamellotti, F. Magrini, D. Cordischi, *J. Mol. Spectrosc.* **1967**, *24*, 270–276.
[112] M. Hitchman, P. Cassidy, *Inorg. Chem.* **1978**, *17*, 1682–1684.
[113] S. Haussühl, R. Leckebusch, K. Recker, *Z. Naturforsch. A* **1972**, *27*, 1022.
[114] M. Mortier, B. Piriou, J. Y. Buzaré, M. Rousseau, J. Y. Gesland, *Phys. Rev. B* **2003**, *67*, 115126.
[115] A. V. Chadwick, S. R. Davis, J. F. de Lima, M. E. G. Valerio, S. L. Baldochi, *J. Phys. Condens. Matter* **1996**, *8*, 10679.
[116] F. Rodríguez, M. Moreno, *J. Chem. Phys.* **1986**, *84*, 692.
[117] B. Villacampa, R. Cases, V. M. Orera, R. Alcalá, *J. Phys. Chem. Solids* **1994**, *55*, 263–272.
[118] A. Mehra, P. Venkateswarlu, *J. Chem. Phys.* **1967**, *47*, 2334.
[119] J. M. García-Lastra, P. García-Fernandez, M. T. Barriuso, J. A. Aramburu, M. Moreno, *J. Phys. Chem. A* **2014**, *118*, 2377–2384.
[120] G. V. Gibbs, D. W. Breck, E. P. Meagher, *Lithos* **1968**, *1*, 275.
[121] L. E. Orgel, *Nature* **1957**, *179*, 1348.
[122] D. Reinen, M. Atanasov, S. L. Lee, *Coord. Chem. Rev.* **1998**, *175*, 91.
[123] J. M. García-Lastra, M. T. Barriuso, J. A. Aramburu, M. Moreno, *J. Phys. Condens. Matter* **2010**, *22*, 155502.
[124] D. S. McClure, *J. Chem. Phys.* **1963**, *38*, 2289–2294.
[125] É. Gaudry, P. Sainctavit, F. Juillot, F. Bondioli, P. Ohresser, I. Letard, *Phys. Chem. Miner.* **2006**, *32*, 710.
[126] O. Schmitz-Du Mont, D. Reinen, *Z. Elektrochem.* **1959**, *63*, 978.
[127] D. Reinen, *Struct. Bonding (Berlin)* **1969**, *6*, 30.
[128] J. M. García-Lastra, M. T. Barriuso, J. A. Aramburu, M. Moreno, *Phys. Rev. B: Condens. Matter Mater. Phys.* **2009**, *79*, 241106.
[129] L. Pauling, *The Nature of the Chemical Bond*, Cornell University Press, Ithaca **1960**, p. 88–91.
[130] M. Pastoureau, *Blue: The History of a Color*, Princeton University Press, Princeton, New Jersey **2001**, pp. 13–23.
[131] H. Berke, *Angew. Chem. Int. Ed.* **2002**, *41*, 2483–2487.
[132] P. García-Fernandez, M. Moreno, J. A. Aramburu, *J. Chem. Educ.* **2016**, *93*, 111–117.
[133] B. C. Chakoumakos, J. A. Fernandez-Baca, L. A. Boatner, *J. Solid State Chem.* **1993**, *103*, 105–113.
[134] J. Karpinski, H. Schwer, I. Mangelschots, K. Conder, A. Morawski, T. Lada, A. Paszewin, *Physica* **1994**, *234*, 10–18.
[135] R. J. Ford, M. A. Hitchman, *Inorg. Chim. Acta* **1979**, *33*, L167–L170.
[136] G. Accorsi, G. Verri, M. Bolognesi, N. Armaroli, C. Clementi, C. Miliani, A. Romani, *Chem. Commun.* **2009**, 3392–3394.
[137] M. Moretti Sala, V. Bisogni, C. Aruta, G. Balestrino, H. Berger, N. B. Brookes, G. M. de Luca, D. Di Castro, M. Grioni, P. G. Medaglia, F. Miletto Granozio, M. Minola, P. Perna, M. Radovic, M. Salluzzo, T. Schmitt, K. J. Zhou, L. Braicovich, G. Ghiringhelli, *New J. Phys.* **2011**, *13*, 043026.
[138] M. G. Clark, R. G. Burns, *J. Chem. Soc. A* **1967**, 1034–1038.
[139] T. Rajaramanan, M. Keykhaei, F. H. Gourji, P. Ravirajan, M. Senthilnanthanan, Ø. Fretteb, D. Velauthapillai, *Mater Adv* **2023**, *4*, 4344.
[140] M. Nicola, R. Gobetto, A. Masic, *Rediconti Lincei Scienze Fisiche e Naturali* **2023**, *34*, 369–413.
[141] M. M. Coimbra, I. Martins, S. M. Bruno, P. D. Vaz, P. J. A. Ribeiro-Claro, S. Rudić, M. M. Nolasco, *Cryst. Growth Des.* **2023**, *23*(7), 4961–4969.
[142] A. Martinelli, E. Sartori, M. Campolucci, M. Ferretti, Z. Hens, F. Locardi, *Chem. Mater.* **2023**, *35*, 9572–9580.
[143] M. Nicola, C. Garino, S. Mittman, E. Priola, L. Palin, M. Ghirardello, V. Damagatla, A. Nevin, A. Masic, D. Comelli, R. Gobetto, *Mater. Chem. Phys.* **2024**, *313*, 128710.
[144] J. M. García-Lastra, J. A. Aramburu, M. T. Barriuso, M. Moreno, *Phys. Rev. B* **2006**, *74*, 115118.
[145] J. M. García-Lastra, M. T. Barriuso, J. A. Aramburu, M. Moreno, *Phys. Rev. B* **2008**, *78*, 085117.
[146] B. Murphy, B. Hathaway, *Coord. Chem. Rev.* **2003**, *243*, 237–262.
[147] M. A. Halcrow, *Chem. Soc. Rev.* **2013**, *42*, 1784–95.
[148] S. E. McLain, M. R. Dolgos, D. A. Tennant, J. F. C. Turner, T. Barnes, T. Proffen, B. C. Sales, R. I. Bewley, *Nat. Mater.* **2006**, *5*, 561–566.
[149] I. Sánchez-Movellán, G. Santamaría-Fernández, P. García-Fernández, J. A. Aramburu, M. Moreno, *J. Phys. Chem. C* **2023**, *127*(33), 16695–16708.
[150] L. J. de Jongh, R. Block, *Physica B + C* **1975**, *79*, 568–593.
[151] H. Bill, *Phys. Lett. A* **1973**, *44*, 101–102.
[152] P. García Fernández, J. A. Aramburu, M. T. Barriuso, M. Moreno, *Phys. Rev. B* **2004**, *69*, 174110.
[153] I. Sánchez-Movellán, J. Moreno-Ceballos, P. García-Fernández, J. A. Aramburu, M. Moreno, *Chem. Eur. J.* **2021**, *27*, 13582–13590.

Manuscript received: January 29, 2024
Revised manuscript received: July 26, 2024
Accepted manuscript online: August 13, 2024
Version of record online: October 6, 2024